HHS Public Access

Author manuscript

Nat Cancer. Author manuscript; available in PMC 2021 July 21.

Published in final edited form as:

Nat Cancer. 2020 November ; 1(11): 1097–1112. doi:10.1038/s43018-020-00121-4.

Multimodal Mapping of the Tumor and Peripheral Blood Immune Landscape in Human Pancreatic Cancer

Nina G. Steele[#1], **Eileen S. Carpenter**[#2], **Samantha B. Kemp**[#3], **Veerin Sirihorachai**[#4], **Stephanie The**[5], **Lawrence Delrosario**[6], **Jenny Lazarus**[6], **El-ad David Amir**[7], **Valerie Gunchick**[8], **Carlos Espinoza**[6], **Samantha Bell**[6], **Lindsey Harris**[9], **Fatima Lima**[6], **Valerie Irizarry-Negron**[6], **Daniel Paglia**[9], **Justin Macchia**[6], **Angel Ka Yan Chu**[5], **Heather Schofield**[6], **Erik-Jan Wamsteker**[2], **Richard Kwon**[2], **Allison Schulman**[2], **Anoop Prabhu**[2], **Ryan Law**[2], **Arjun Sondhi**[2], **Jessica Yu**[2], **Arpan Patel**[2], **Katelyn Donahue**[4], **Hari Nathan**[6], **Clifford Cho**[6], **Michelle A. Anderson**[2], **Vaibhav Sahai**[8], **Costas A. Lyssiotis**[3,4,9], **Weiping Zou**[6], **Benjamin L. Allen**[1], **Arvind Rao**[4,5,10,11], **Howard C. Crawford**[3,4,9,*], **Filip Bednar**[6,*], **Timothy L. Frankel**[6,*], **Marina Pasca di Magliano**[1,3,4,6,*]

[1]Department of Cell and Developmental Biology, University of Michigan, Ann Arbor, MI 48109, USA.

[2]Department of Internal Medicine, Division of Gastroenterology, University of Michigan, Ann Arbor MI 48109, USA.

[3]Molecular and Cellular Pathology Graduate Program, University of Michigan, Ann Arbor, MI 48109, USA.

[4]Cancer Biology Program, University of Michigan, Ann Arbor, MI 48109, USA.

[5]Department of Computational Medicine and Bioinformatics, University of Michigan, Ann Arbor, MI 48109, USA.

[6]Department of Surgery, University of Michigan, Ann Arbor, MI 48109, USA.

[7]Astrolabe Diagnostics, Inc., Fort Lee, NJ, 07024, USA.

[8]Department of Internal Medicine, Division of Hematology and Oncology, University of Michigan, Ann Arbor, MI 48109, USA.

[9]Department of Molecular and Integrative Physiology, University of Michigan, Ann Arbor, MI 48109, USA.

[*]Co-corresponding authors. marinapa@umich.edu (MPdM); timofran@med.umich.edu (TF); filipb@umich.edu (FB); howcraw@med.umich.edu (HC).

Author contributions:

MPdM directed the study. TF, FB, and HC assisted with study design and analysis. MPdM, NS, EC, and SK developed the study concept, and were responsible for study design. JL, LD, VIN and SB stained and analyzed and TLF coordinated the multiplex immunohistochemistry. VG, EC, EJW, RK, AS, AP, RL, JY, AP, HN, CC, MA, HS procured human tissue and assisted with clinical data collection. VG and EC maintained the database of human biospecimens. NS, EC, SK, DP, JM, CE, FL processed samples for CyTOF. EC, VS, JM, CE, DP, LH processed samples for single cell RNA sequencing. FB developed an R pipeline for CyTOF analysis. EDA analyzed CyTOF PBMC data. AR, ST and AC developed bioinformatic analysis pipelines and carried out the interactome analysis. VRS, NS, SK, KD analyzed single cell RNA sequencing data. NS, SK, EC analyzed the CyTOF data. VS, CL, BLA, AR, HS, WZ, HC, FB, TF, CC, KD, EDA, provided study guidance and feedback on the manuscript. NS, EC, SK, and MPdM wrote the manuscript, which was then edited by all the co-authors. All the co-authors approved the final version of the manuscript prior to submission.

Competing interests: The authors have declared that no conflict of interest exists.

[10]Michigan Institute of Data Science (MIDAS), University of Michigan, Ann Arbor, MI 48109, USA.

[11]Department of Radiation Oncology, University of Michigan, Ann Arbor, MI 48109, USA.

[#] These authors contributed equally to this work.

Abstract

Pancreatic ductal adenocarcinoma (PDA) is characterized by an immune-suppressive tumor microenvironment that renders it largely refractory to immunotherapy. We implemented a multimodal analysis approach to elucidate the immune landscape in PDA. Using a combination of CyTOF, single-cell RNA sequencing, and multiplex immunohistochemistry on patient tumors, matched blood, and non-malignant samples, we uncovered a complex network of immune-suppressive cellular interactions. These experiments revealed heterogeneous expression of immune checkpoint receptors in individual patient's T cells and increased markers of $CD8^+$ T cell dysfunction in advanced disease stage. Tumor-infiltrating $CD8^+$ T cells had an increased proportion of cells expressing an exhausted expression profile that included upregulation of the immune checkpoint *TIGIT*, a finding that we validated at the protein level. Our findings point to a profound alteration of the immune landscape of tumors, and to patient-specific immune changes that should be taken into account as combination immunotherapy becomes available for pancreatic cancer.

Graphical Abstract

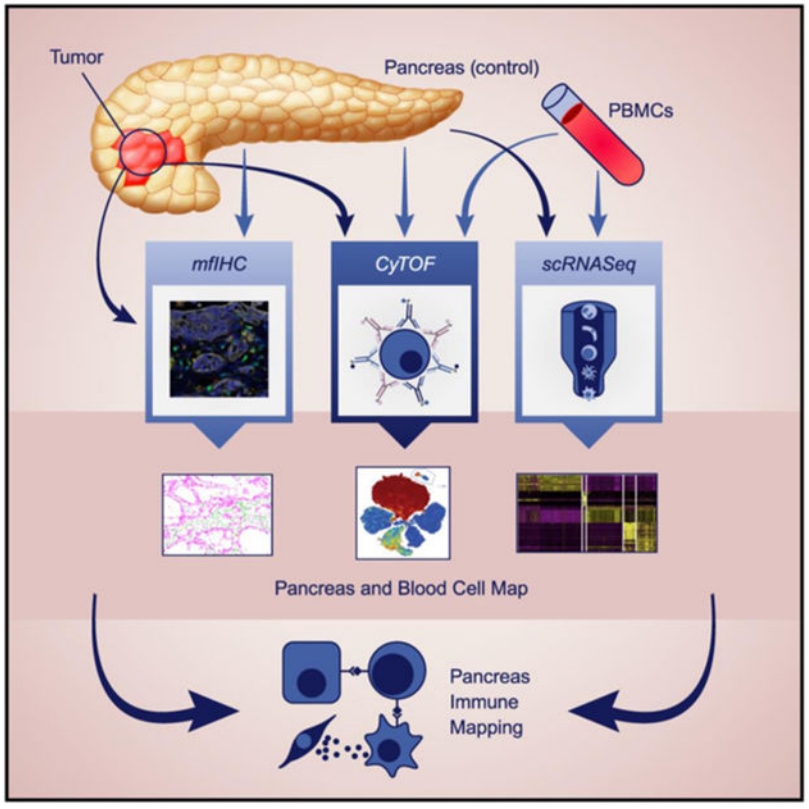

Keywords

Single-cell RNA sequencing; tumor immunology; CD8$^+$ T cells; immune checkpoints; TIGIT; pancreatic cancer

Introduction

Pancreatic ductal adenocarcinoma (PDA), one of the deadliest human malignancies, is distinguished by an extensive and complex tumor microenvironment (TME) containing abundant infiltrating immune cells. Immunotherapy clinical trials using checkpoint inhibitors PD-1 and CTLA4 as single agents have been unsuccessful [1, 2], but recent clinical trials using combination of immune regulatory agents have shown positive initial results (NCT02588443), indicating the need to target multiple components of the stroma and better understand the immune landscape of human PDA. The prevalence of CD8$^+$ T cells varies across patients [3]. Deconvolution of bulk RNA sequencing data from The Cancer Genome Atlas (TCGA) stratified tumors based on their cytolytic index, including a high cytolytic index group [4]. These data indicate that the CD8$^+$ T cell landscape in pancreatic tumors might be more complex than previously believed, and the mechanisms of immune suppression may vary across patients. While pancreatic cancer is most often diagnosed when locally invasive or metastatic, most existing datasets are limited to surgical samples representing earlier stages of the disease.

The presence and distribution of cytotoxic T cells in PDA has important prognostic correlations; CD8$^+$ T cells in proximity to PDA cells correlate with increased overall survival [5]. Further, analysis of rare long-term PDA survivors revealed persistence of T cell clones specific to tumor antigens [6]. Conversely, infiltration of myeloid cells, specifically tumor associated macrophages, negatively correlates with prognosis [7], consistent with an immune-suppressive role of these cells [8]. CD4$^+$ T cells are abundant within tumors, with a prevalence of regulatory T cells [9]; their nature in human PDA is currently poorly understood. Similarly, our understanding of other immune cell types within tumors is limited.

Here, we used multiple, complementary approaches [mass cytometry (CyTOF), single-cell RNA sequencing (scRNA seq), and multiplex fluorescent immunohistochemistry (mfIHC)] to investigate the immune landscape of pancreatic tumors from a collection of samples that included both surgical and fine needle biopsy samples, as well as matched patient blood (graphical abstract). Our work adds an in-depth immune characterization to complement recent single cell characterization on pancreatic tumor cells [10, 11] and cancer associated fibroblasts [12, 13]. We observed that immune landscapes in each individual patient were heterogeneous, although some common features emerged. Cytotoxic T cells in patients displayed an exhausted gene expression signature, which was progressively more pronounced in advanced disease. The specific combinations of immune checkpoint genes expressed in each patient's CD8$^+$ T cells was unique. Tumor infiltrating CD8$^+$ T cell had a higher proportion of cells expressing genes previously associated with T cell exhaustion, and these cells had enriched expression of the immune checkpoint *T-cell immunoglobulin and*

ITIM domains (*TIGIT*) [14]. Predicted interaction analysis [15, 16] revealed multiple potential cellular interactions upregulated in tumors compared with non-malignant tissue. Overall, our study provides a wealth of hypothesis-generating data to benefit the PDA community at large.

Results

CyTOF and multiplex immunohistochemistry mapping reveal heterogeneous immune infiltration in human pancreatic cancer.

To map the immune infiltration in pancreatic cancer, we performed CyTOF on 10 pancreatic tumor samples and 8 samples from non-malignant pancreas specimens [Whipple pancreaticoduodenectomy (n=2), distal pancreatectomy (n=4), partial pancreatectomy (n=1) or endoscopic fine needle biopsy (n=3)]. Clinical pathology review provided the diagnosis for samples (Extended Data Fig. 1A); histology of surgical specimens is shown in Extended Data Fig. 1B. Our validated antibody panel contained 30 immune markers (Supplemental Table 1) [17]. We used the Astrolabe Cytometry platform for batch correction to account for differences in the timing of sample acquisition, and selected live singlets for downstream analysis [18, 19].

Principal component analysis (PCA) showed a minor shift between adjacent or normal pancreas and tumor samples (Fig. 1A), indicating differences in immune cell composition. To visualize the distribution of cell populations within individual samples, we utilized unbiased hierarchical clustering algorithms [18], along with supervised annotation (Fig. 1B,C and Extended Data Fig. 1C,D). While adjacent/normal samples contained mostly non-immune cells, tumor samples had an abundance of immune cells (Fig. 1C). Multiple immune populations were elevated in tumor samples: myeloid cells, B cells, NK cells, $CD4^+$ T cells, regulatory T cells and $CD8^+$ T cells (Fig. 1D and Extended Data Fig. 1E). We observed an inverse correlation between the percentage of myeloid cells and $CD8^+$ T cells (Fig. 1E), consistent with previous observation in mouse models and in agreement with the notion that myeloid cells are a key immunosuppressive component in pancreatic cancer [3, 9, 20–22].

To measure immune composition in undisturbed tissue and define the spatial relationships between immune cells in the microenvironment, we performed seven-color multiplex fluorescent immunohistochemistry (mfIHC) on a formalin fixed paraffin embedded tissue tumor microarray (TMA) comprised of 71 PDA and 34 chronic pancreatitis samples, as previously described [23] (Extended Data Fig. 1F). Representative images from individual samples are shown in Fig. 1F, Extended Data Fig. 1G–H. Chronic pancreatitis samples contained a higher epithelial cell component than the PDA samples. Conversely, immune cell infiltration was more abundant in PDA tissue (Fig. 1G). In agreement with our CyTOF analysis, mfIHC demonstrated an increase in Tregs ($FOXP3^+$) and macrophages ($CD163^+$). However, unlike in the CyTOF data, $CD8^+$ T cells did not change (Fig. 1G), likely reflecting differences in the control tissues (chronic pancreatitis versus adjacent/normal pancreas). Individual patient tumors were variable in terms of $CD8^+$ T cell infiltration. As in the CyTOF data, we observed a negative correlation between $CD8^+$ T cells and myeloid cells in PDA samples (Fig. 1H and 1E) [7, 9], supporting a key immunosuppressive role of this cell

population [20, 24–29]. Overall, our data show a complex microenvironment and considerable variability across individual patients.

Single cell RNA sequencing reveals a complex immune landscape with heterogeneous expression of immune checkpoints and ligands in the pancreatic cancer microenvironment.

We performed single cell RNA sequencing (scRNA seq) on 16 PDA samples, including surgical (n=6) and fine needle biopsy specimens (n=10) (Extended Data Fig. 2A). All the patients were treatment-naïve at the time of sample acquisition. We also included three non-malignant pancreas samples (1196, 1258, 19732) from patients undergoing surgery for duodenal adenoma, ampullary carcinoma, or adjacent to PDA, respectively, where an uninvolved portion of pancreas was included in the resection (as determined by pathologic evaluation). To capture a window into the systemic immune response in PDA patients, we also collected peripheral blood mononuclear cells (PBMCs) from these patients and healthy subjects (Extended Data Fig. 2A, *right panel*).

In total, we sequenced 8541 cells from adjacent/normal samples and 46,244 from PDA, while from the blood samples we sequenced 14,240 cells from 4 healthy subjects, and 55,873 cells from 16 PDA patients. To define and visualize cell subpopulations, we batch corrected our tumor and blood sequencing samples (Extended Data Fig. 2B) and then used unbiased clustering and a dimensionality reduction through Uniform Manifold Approximation and Projection (UMAP) (Fig. 2A and Extended Data Fig 3A). We identified each subpopulation based on published lineage markers (Fig. 2B and Extended Data Fig. 3B). We observed variability in the total immune cell composition of individual tumors, and in the relative abundance of individual immune cell components similar to CYTOF and mfIHC data (Extended Data Fig. 2C and 2D).

We identified abundant pro-inflammatory cells in the PDA microenvironment including $CD8^+$ T cells and natural killer cells (NK) (Fig. 2A). To gather insight into the possible mechanisms preventing anti-tumor immune responses, we profiled average expression of immune checkpoint receptors and ligands by cell type, both in tumors and PBMCs of PDA patients (Fig. 2C and Extended Data Fig. 3C). We observed expression of multiple immune checkpoint receptors in T and NK cell subsets, while myeloid populations were enriched for their corresponding ligands (Fig. 2C). $CD8^+$ T cells had elevated *ICOS, TIGIT, PDCD1* and *LAG3*, among others, but relatively low expression of *CTLA4*. *CTLA4*, as well as all other checkpoints except for *LAG3*, was high in $CD4^+$ T cells. NK cells also had elevated *CD47, TIGIT, TNFRSF18* and *LAG3*, and modest expression of *PDCD1*. The expression of checkpoint ligands was heterogeneous, with epithelial cells mainly expressing *PVR* and *LGALS9* (encoding for *PVR* and *GALECTIN 9*, ligands for *TIGIT* and *HAVCR2*(*TIM3)* respectively). Myeloid and dendritic cells expressed several genes encoding checkpoint ligands, including *SIRPA, LGALS9, PVR*, and *ICOSLG* (Fig. 2C). Similarly, in PBMC samples, $CD4^+$ T cells, $CD8^+$ T cells and NK cells had elevated expression of multiple immune checkpoint receptors (*TIGIT* was elevated in all three cellular compartments), and granulocytes, monocytes and B cells, plasma cells and dendritic cells expressed the ligands (Extended Data Fig. 3C). We also detected expression of immune checkpoint ligands in

other non-immune cell types, which included fibroblasts, endocrine, and endothelial cells (Fig. 2C). Our single cell data revealed a complex, patient-specific landscape of immune checkpoint ligand and receptor expression across multiple immune and non-immune cell types.

Tumor-infiltrating CD8+ T cells have a distinct gene expression profile, with progressive dysfunction in advanced disease.

Cytotoxic T cells are a fundamental component of anti-tumor immune responses and the target of immunotherapy (for review see [30]). To gather deeper insight into the functional status of tumor-infiltrating $CD8^+$ T cells, we investigated their transcriptional profile. To investigate patient-specific variability, we mapped the average expression of immune checkpoint receptors in $CD8^+$ T cells in each individual patient's tumor and blood samples (Fig. 2D and Extended Data Fig. 3D). Infiltrating $CD8^+$ T cells expressed markedly distinct immune checkpoint profiles in individual patient samples, both in tumors and blood (Fig. 2D and Extended Data Fig. 3D). In tumor samples, *LAG3* was elevated in patients 1141, 1294, 1261 and 1229. Patient 1229 (locally advanced) also had high expression of *ICOS, CTLA4, TIGIT* and *CD47*. Conversely, patient 1261 (also locally advanced), had elevated *CD27, LAG3, PDCD1, HAVCR2, TNFRSF18, CSF1, TIGIT, CD40LG, CD47* and *CD28*, but not *CTLA4*. The immune checkpoint landscape did not cluster by disease stage, and while some metastatic patients had high expression of multiple immune checkpoints (3210) others expressed only a limited subset (1253). Analysis of circulating $CD8^+$ T cells revealed a similarly complex landscape, but no clear overall correlation in the expression of individual checkpoints between patient tumor and blood T cells at a gene expression level (Extended Data Fig. 3D).

We then investigated tumor-infiltrating $CD8^+$ T cells compared to $CD8^+$ T cells in normal/adjacent tissue. By functional annotation, we observed pathways relating to cell cytotoxicity, chemokine signaling, T cell receptor signaling, and antigen processing were significantly enriched in PDA samples, compared to adjacent/normal tissue $CD8^+$ T cells, an indication that immune responses had been elicited in the tumors (Fig. 2E). We performed unbiased clustering of the $CD8^+$ T cell gene expression signatures in patients. Circulating $CD8^+$ T cells gene expression patterns did not clearly segregate by disease stage (Extended Data Fig. 3E). We then performed an unbiased differential expression analysis on the tissue-infiltrating $CD8^+$ T cells in tumors versus adjacent/normal tissue. This analysis revealed distinct expression patterns in healthy versus tumor infiltrating total $CD8^+$ T cells (Fig 2F). We noted that the $CD8^+$ T cells in adjacent/normal samples clustered together, while tumor-infiltrating $CD8^+$ T cell signatures spanned a spectrum in individual samples. Some tumor signatures partially resembled non-malignant tissue and others were greatly diverging. Interestingly, upon clinical annotation, we discovered that the divergence from the normal signature was more pronounced in samples from advanced disease stage. When we considered which genes were differentially expressed across the groups, we observed an increase in T cell activation and trafficking markers (*GZMB, GZMA, KLF2*) [3, 4, 31] in tumor $CD8^+$ T cells, compared to adjacent/normal tissues. Further, T cell exhaustion markers such as *EOMES* and *GZMK* were low in healthy $CD8^+$ T cells, and elevated in the majority of tumor $CD8^+$ T cell samples [32, 33]. The only immune checkpoint receptor

identified as differentially overexpressed in tumor-infiltrating $CD8^+$ T cells, compared to $CD8^+$ T cells in adjacent/normal tissue, was *TIGIT*, a gene encoding a receptor belonging to the Ig superfamily [14]. Overall, comparison of the transcriptional profile of tumor and adjacent/normal infiltrating $CD8^+$ T cells revealed unique profiles of expression of immune checkpoint genes in individual patients. However, some common features emerged, such as expression of activation markers, as well as an exhausted gene expression signature which progressively increased with advanced disease stage.

Tumor infiltrating $CD8^+$ T cells include an expanded exhausted population characterized by TIGIT expression.

Distinct populations of tumor infiltrating $CD8^+$ T cells have been described [34]. Given the progressive dysfunction of tumor-infiltrating $CD8^+$ T cells, we hypothesized that the transcriptional profile shift might be caused by changes in $CD8^+$ populations. By unbiased clustering, we distinguished 6 populations of *CD8A*-expressing T cells in both adjacent/normal and PDA samples (Fig. 3A). To identify sub-populations, we plotted the top expressed genes per cluster (Fig. 3B), and compared them with published signatures of $CD8^+$ T cells subtypes [32]. We identified two populations of effector $CD8^+$ T cells (T_{eff}), expressing *PRF1* and *GZMB*; a population of likely memory (mem)/ precursor effector (pec) $CD8^+$ T cells ($T_{mem/pec}$) expressing *CCR6* [35]; and two populations of exhausted $CD8^+$ T cells (T_{ex}) expressing *EOMES*, *GZMK*, and *TIGIT* (Fig. 3C, Extended Data Fig. 4A and average expression heatmap in Extended Data Fig. 4C). Interestingly, comparison of tumor infiltrating versus adjacent/normal $CD8^+$ T cells revealed a relative increase in exhausted T cells and memory T cells, with converse reduction of effector T cell levels (Fig. 3D and Extended Data Fig. 4B). We then examined expression of immune checkpoints and immune activation markers across $CD8^+$ T cell subsets, and observed uniform expression of *PDCD1*, *HAVCR2* and *LAG3* (Fig. 3C), while *TIGIT* was enriched in exhausted and memory $CD8^+$ T cells. We found that 13.3% of effector $CD8^+$ T cells, compared to 44.2% of exhausted $CD8^+$ T cells expressed TIGIT. To compare gene expression changes within distinct clusters of $CD8^+$ T cells, we performed two separate differential expression analyses. We first compared PDA effector $CD8^+$ T cells to adjacent/normal effector $CD8^+$ T cells, and we found that *GZMA* and *GZMB* were higher in tumor infiltrating effector $CD8^+$ T cells, suggesting T cell activation (Fig. 3E). *RORA* expression, a marker associated with effector T cells, was also upregulated [32] (Fig. 3E), consistent with an ongoing immune response. We then compared PDA exhausted $CD8^+$ T cells to adjacent/normal exhausted $CD8^+$ T cells and tumor infiltrating exhausted $CD8^+$ T cells had higher expression of *EOMES* and *KLF2*, markers of exhaustion [32] (Fig. 3F).

Our data suggest that exhausted $CD8^+$ T cells are abundant in pancreatic tumors, and that their exhausted phenotype is more profound than the equivalent population in adjacent/normal tissue. Further, *TIGIT* was the sole immune checkpoint receptor that specifically defined exhausted $CD8^+$ T cells.

A complex landscape of NK and $CD4^+$ T cells cell subsets in pancreatic cancer.

Similar to effector $CD8^+$ T cells, NK cells display cytotoxic activity and express immune checkpoint receptor (Fig. 2C), however these cells are not well defined in human PDA [36].

Unsupervised sub-clustering of NK cells revealed three populations (Fig. 4A and 4B). Along with the three NK cell subsets, we found two additional populations that we labeled cluster 1 and 2, which expressed *NKG7, CD3E*, and *CD8A*. While these cells did not cluster with the CD8 T cells based on their transcriptional profile, they could potentially be highly cytolytic CD8 T cells expressing some NK markers [37, 38]. A "NK" cell population expressing *CD8A* was identified in a recent PDA scRNA-seq paper [12]. Highly variable gene expression analysis highlighted differences among subpopulations (Fig. 4B). In NK subsets we detected expression of markers of antigen presentation (*HLA-DRA*), cytolytic activity (*PRF1, GZMB*), and chemokines/chemokine receptors (*CCL3, IL7R*), in agreement with a recently published characterization of human NK cells by single cell RNA sequencing [39]. NK cluster 1 was enriched for immune checkpoint *HAVCR2*, while NK cluster 3 expressed high levels of immune checkpoint *TNFRSF4* (Fig. 4B and 4C). We then performed differential gene expression analysis and unbiased clustering of individual patient samples to compare tumor infiltrating NK cells with NK cells in non-tumor tissue. The signatures of tumor-infiltrating and non-tumor NK cells were not as divergent as was the case for $CD8^+$ T cells, and, with one exception (1324), resectable tumor samples clustered closely with the non-tumor samples (Fig. 4D). However, advanced disease samples had a different expression signature than healthy counterparts, with increased expression of activation markers such as *GZMA* and elevated expression of two immune checkpoint genes, *TIGIT* and *HAVCR2*. The role of NK cells in PDA is not well understood; our findings set the stage for future functional studies on the role of NK cells in this disease.

We then investigated $CD4^+$ T cells, a complex population that includes regulatory T cells, and plays a fundamental role in regulating pancreatic carcinogenesis [40–42]. Unlike the $CD8^+$ T and NK cells, we could not perform differential expression on $CD4^+$ T cells as we did not capture enough cells from adjacent/normal tissue samples; instead we focused on studying the tumor-infiltrating component. We identified 13 transcriptionally distinct populations of $CD4^+$ T cells, although many of the different clusters tended to merge together (Fig. 4E). A highly enriched gene analysis of $CD4^+$ subsets revealed expression of naïve T cell markers *CCR7* and *SELL* [43] in cluster 0 and expression of regulatory T cell marker *FOXP3* in cluster 3 (Fig. 4F). As expected, based on previous studies, *CTLA4* was highly expressed within Tregs [44] (Fig. 4G). Specific immune checkpoint genes were highly expressed in individual clusters, such as *TNFRSF18* and *PDCD1. TIGIT* appeared as a top expressed gene in Tregs (Fig. 4F), although it was also expressed in other clusters more sparsely (Fig. 4G). The other clusters did not correspond to known subsets of $CD4^+$ T cells, and were relatively similar to one another, a possible reflection of low transcriptional activity of non-Treg $CD4^+$ T cells. Taken together, these analyses suggest multiple immune checkpoint receptors are expressed in $CD4^+$ and NK cell subsets. In particular, the immune checkpoint *TIGIT* was differentially overexpressed on tumor-infiltrating PDA $CD8^+$ T cells, regulatory T cells and NK cells.

Myeloid and dendritic cells are an important source of immune checkpoint ligands in human PDA.

We next analyzed myeloid cells, which are an important source of immune checkpoint ligands in PDA. By unbiased clustering, we identified 6 transcriptionally distinct populations

of myeloid cells. (Fig. 5A). We observed an abundant granulocyte population expressing *CXCR1* and *CXCR2, FCGR3B* and *S100A8* (Fig. 5B). Consistent with previous studies [12, 25], we detected resident macrophages and alternatively activated macrophages (*MARCO*$^{+}$), and classical monocytes (Fig. 5A and B). We also observed an additional myeloid population, denoted as alternatively activated macrophages 2, that resembled alternatively activated macrophages and was uniquely defined by abundant expression of *CHIT1* and multiple immune checkpoint ligands (Fig. 5A, 5B and Extended Data Fig. 5A). We next mapped immune checkpoint ligand expression within specific myeloid compartments and observed heterogeneous expression of immune checkpoints in specific clusters (Fig. 5C). Differential expression analysis between adjacent/normal and tumor-infiltrating myeloid sub-clusters revealed multiple upregulated checkpoint ligands. *LGALS9*, the ligand for *HAVCR2* (encoding for TIM3), was significantly increased within alternatively activated macrophages, while *SIRPA*, the ligand for *CD47*, was higher in PDA granulocytes compared to granulocytes in adjacent/normal tissue (Fig. 5D). *PVR*, the ligand for *TIGIT* was enriched in total macrophages (Fig. 5D). Average expression heatmaps of macrophages (Extended Data Fig. 5B) and granulocytes (Extended Data Fig. 5C) demonstrated that the expression of immune checkpoint ligands was highly variable in individual patients.

Dendritic cells (DCs) cells are professional antigen presenting myeloid cells, and support anti-tumor activity by stimulating T cells; their relative rarity in PDA is one of the potential causes for ineffective immune responses in this disease [45]. Clustering analysis revealed multiple populations of tumor-infiltrating DCs (Fig. 5E). We found two populations of plasmacytoid DCs (*IRF8, GZMB*) and two populations of Langerhans-like DCs (*CD207*, *CD1A*) as previously described [12] (Fig. 5F and 6A). Langerhans-like DC2 had robust expression of *IL22RA2*, also known as IL22BP, and the IL-22-IL22BP axis is known to be a crucial mediator of tumorigenesis in the colon [46] and pancreas [47]. We also detected a population of conventional DC1s (*CLEC9A, IRF8*) [12, 48], and two additional populations of potential conventional DC2s that expressed immune checkpoint ligand *SIRPA* (Fig. 5F and 6A). We also detected two unique populations of activated DCs (*LAMP3*, *CCL22*) [12] (Fig. 5F and 6A). We then plotted the average expression of known immune checkpoint ligands in the different DC subsets. We discovered that activated DC1 had elevated expression of nearly all the immune checkpoint ligands, including *PVR* (Fig. 6B), suggesting that in pancreatic tumors some subsets of DCs may be immunosuppressive [49].

Mapping predicted interactions and tissue heterogeneity in pancreatic cancer samples by single cell sequencing.

To explore potential cross-talk between T/NK and myeloid populations, we applied a predicted interaction algorithm [15] based on known ligand-receptor (LR) pairs interacting with high affinity [50]. We curated the list to specifically add immune checkpoints and limit the receptor-ligand pairs to cytokines, chemokines and specific signaling pathways [for a comprehensive list, see Supplemental Table 5]. We first plotted all the receptor-ligand interactions that were statistically higher in tumor versus non-malignant samples, based on the level of ligand expression, and observed a complex landscape of potential interactions involving multiple cell types (Extended Data Fig. 5D). We then visualized upregulated ligands in macrophages (Fig. 6C), granulocytes (Fig. 6D), dendritic cells (Fig. 6E),

endothelial cells (Fig. 6F) and epithelial cells (Fig. 6G) and mapped the predicted binding partners in CD4, CD8, and NK cells. Among interactions upregulated in cancer compared to adjacent/normal, we detected known putative immune suppressive interactions, such as those mediated by the chemokine receptors *CXCR2* in granulocytes and *CCR2* in macrophages [25, 26]. Predicted interactions mediated by *IL1A* and *IL1B* with their receptor encoding genes *IL1R1* and *IL1R2* were also upregulated, consistent with their known roles in pancreatic cancer [12, 51, 52]. Multiple putative interactions linked T and NK cells to myeloid immune checkpoint ligands, which is consistent with a key role for myeloid cells in establishing immune suppression in pancreatic cancer (for review see [8]). Predicted immune checkpoint-mediated interactions such as *ICOS/ICOSLG* and *SIRPA/CD47* were among those upregulated in pancreatic cancer compared to healthy/adjacent tissue. *TIGIT/PVR* interactions were elevated between macrophages and $CD4^+$ T cells, $CD8^+$ T cells and NK cells (Fig. 6C). Interestingly, the putative *TIGIT/PVR* interaction was also elevated between tumor endothelial and epithelial cells, T cell and NK cell subsets (Fig. 6F, G). We then endeavored to investigate the expression of other genes involved in the TIGIT pathway. We investigated the expression of TIGIT's costimulatory counter receptor, DNAM1 (CD226), which competes for PVR and PVRL2 and promotes T cell activation [53]. We found that while TIGIT was significantly increased on PDA $CD8^+$ T cells (P= 4.8E-32), CD226 expression was not altered in $CD8^+$ T cells between adjacent/normal and PDA cells (Fig. 6H). CD96 and PVRIG act similarly to TIGIT, inhibiting T cell activation. Expression analysis showed that mRNA levels of these receptors were not altered between adjacent/normal and PDA $CD8^+$ T cells (Fig. 6H). PVRL2 encodes a second ligand for TIGIT, although it binds with a lower affinity compared to PVR [54]. We detected expression of *PVRL2* in epithelial, myeloid, and endothelial cells (Fig. 6I). TIGIT, CD96, PVRIG, and CD226 were mainly expressed by T and NK cells in PDA tissue (Fig. 6I). We then investigated the Adenosine pathway, because of its immune suppressive role [55]. We profiled this pathway in tumor samples and found expression of the adenosine receptor *ADORA1* in epithelial and mast cells, *ADORA2B* in epithelial, mast cells, and dendritic cells, ADORA3 in dendritic, mast, and myeloid cells (Extended Data Fig. 5E).

The expression of multiple immune checkpoints has been previously described in pancreatic cancer [4]. Since a deconvolution approach was used, the specific immune cell types expressing receptors and ligands could not be assessed. In contrast, our analysis provides a comprehensive view of the multiple, redundant potential immune suppressive interactions within the pancreatic cancer microenvironment.

TIGIT protein expression is increased on T and NK cells in pancreatic cancer, and its expression in the tumors correlates with matched blood.

To determine whether mRNA expression of immune checkpoints was reflected by protein levels, we performed mass cytometry on tumor and normal/adjacent uninvolved tissue samples (Fig. 7A). TIGIT expression was elevated in tumor-infiltrating $CD8^+$ T cells in the majority of samples, albeit not all, while PD1 and LAG3 were not significantly altered (Fig. 7A). Interestingly, we detected an increase in expression in PD-1 ligand, PD-L1, in $CD68^+$ macrophages from PDA patients (Extended Data Fig. 7B). CTLA4 expression was significantly increased in $CD4^+$ T cells in most PDA samples versus adjacent/normal tissues

(Fig. 7B). TIGIT$^+$ CD4$^+$;CD25$^+$ T cells were more frequent in PDA samples, compared to controls (Fig. 7B). Similarly, TIGIT$^+$ NK cells (CD56$^+$) were more frequent in PDA, although this finding is limited by the small number of samples analyzed (Fig. 7C). In one patient, where matched tumor and uninvolved adjacent tissue were analyzed, we observed a higher frequency of TIGIT expression on both CD8$^+$ and CD4$^+$ T cells in the tumor (Fig. 7D). We then performed immunostaining for both TIGIT and PVR on patient tissue *in situ* (Fig. 7E) and observed TIGIT in CD8$^+$ T cells, and PVR (red) in epithelial and stromal cells (Fig. 7E and single channels shown in Extended Data Fig. 7A).

Lastly, as we observed that TIGIT was commonly upregulated in tumors, we investigated whether protein expression of TIGIT in blood correlated with the individual patient's tumor, an attractive possibility given the relatively easy accessibility of blood samples. We performed CyTOF on the peripheral white blood cell (PBMC) component in 36 pancreatic cancer patients, 18 healthy volunteers, and 8 patients with chronic pancreatitis (Extended Data Fig. 6A). Cellular subtyping and frequency of circulating immune cells present are shown in Extended Data Fig. 6B–E. Principal component analysis failed to show any major distinction between our three patient populations (Extended Data Fig. 6G). Blood from both PDA and chronic pancreatitis patients had fewer circulating CD8$^+$ T cells, but higher expression of TIGIT CD8$^+$ T cells (Fig. 7F, 7G and Extended Data Fig. 6F). PD1 and CTLA4 protein expression was elevated in PDA circulating CD8$^+$ and CD4$^+$ T cells, respectively, compared to healthy subjects (Fig. 7G). We then analyzed the subset of patients for whom we had matched mass cytometry of tumor and PBMCs and found a positive correlation of TIGIT expression, but not PD1 expression, in CD8$^+$ T cells (Fig. 7H and I). Thus, different immune checkpoint molecules are prevalent in individual patients, and further validation of potential targets, including TIGIT, is warranted.

Discussion

Recent reports examining gene expression in pancreatic tumors by scRNAseq or high content *in situ* hybridization have largely focused on the complexity of the fibroblast populations, [12, 13, 56] however the heterogeneity of the immune reaction in PDA at a single cell level remained unclear. We have used a multi-modal approach combining CyTOF [17, 19], multiplex immunohistochemistry, and scRNA seq to map the immune infiltration, as well as the systemic immune response through patient blood, in human PDA [57].

Multiparameter mapping of the TME demonstrated a highly heterogeneous immune infiltration in individual patients, consistent with previous reports [3], suggesting that immune-modulatory therapies should potentially be targeted to specific individuals based on their checkpoint expression profile within tumors. Both CyTOF and mfIHC also revealed an inverse correlation between infiltration of myeloid and CD8$^+$ T cells. scRNA seq analysis suggests that CD8$^+$ T cells express markers of exhaustion at levels that increase in advanced stages of disease, consistent with a recent study of peripheral T cells in pancreatic cancer patients showing diminished fitness [58]. Importantly, we included fine needle biopsy samples for both single cell sequencing and CyTOF, which allowed us to study the immune infiltration in patients with unresectable advanced stages of disease. These tumors included

$CD8^+$ T cells with a more pronounced exhaustion signature compared with early stage patients, a possible indication of progressive immune dysfunction.

We found differential expression of *TIGIT*, both at the gene and at the protein level, in patient $CD8^+$ T cells. We chose to focus on TIGIT in particular as one example of an immune checkpoint ligand/receptor pair given our ability to evaluate this relatively understudied checkpoint across multiple modalities. *TIGIT* expression was enriched specifically within $EOMES^{high}$ $CD8^+$ T cells, or exhausted T cells, similar to recent findings in human prostate, bladder, and kidney cancer [34]. *TIGIT* was also elevated in NK cells within the tumor, where its role is less understood, although there is at least some evidence TIGIT inhibition in NK cells might be beneficial [59]. Elevated *TIGIT* expression is a feature of Tregs, and again its role in this cell population is not well understood. However, it has been proposed that inhibition of TIGIT on Tregs may suppress the secretion of the immunosuppressive cytokine IL-10 [14]. The expression of TIGIT, and other immune checkpoint receptors in multiple cellular compartments, as well as the observation that expression of immune checkpoints is highly heterogeneous across patients, will have to be further investigated as new combination immunotherapy approaches are devised for preclinical testing. Further, it is interesting to note that multiple cellular compartments express a variety of immune checkpoint ligands in a similar heterogeneous manner. At the protein level, we validated that PVR, the ligand for TIGIT, was expressed in tumor, endocrine, and endothelial cells (while low in non-malignant acinar cells). PVR and other immune checkpoint ligands were also upregulated in myeloid subsets, supporting the notion of myeloid cells as key mediators of immune suppression in PDA. Intriguingly, TIGIT protein expression in the blood correlated with TIGIT expression in the tumors of individual patients, although a similar correlation was not observed for other immune checkpoints such as PD-1. Of note, while functional studies on the role of TIGIT in different patients and different cellular compartments within each tumor are still needed, TIGIT blocking agents are available and are currently being evaluated in clinical trials [60].

In summary, our study provides a multimodal characterization of the immune landscape in PDA, highlights the complexity of this disease in human patients, and provides a resource for future functional studies.

Methods

Study Approval and Patient Consent

Patient Selection/Sample procurement: Medical chart review was used to screen for potential study patients with pancreatic disease at the University of Michigan. Fine needle biopsies: Patients over the age of 18 referred for diagnostic endoscopic ultrasound of a pancreas mass lesion suspected of PDA were consented according to IRB HUM00041280 or HUM00025339. Up to 2 extra passes using at 22 Gauge SharkCore™ needle were taken for research after biopsy obtained for clinical use. Surgical specimens: Surgical specimens of either tumor tissue or adjacent normal pancreas were obtained from patients referred for Whipple procedure or distal pancreatectomy according to IRB HUM00025339. Blood collection: Up to 40 cc of whole blood were collected pre-procedurally or intra-operatively for all patients consented. For patients not undergoing interventional procedures (i.e.

chemotherapy visit), only whole blood was collected. Supplemental Table 2 contains extended clinical data associated with clinical samples.

Multiplex fluorescent immunohistochemistry (mfIHC) imaging, cell segmentation, and basic phenotyping

Images were taken using the Mantra™ Quantitative Pathology Work Station (Akoya Biosciences) as described in the Online Methods.

Cytometry Time-of-Flight (CyTOF) Immune Phenotyping and Data Analysis

For CyTOF, we collected 8 samples from non-malignant pancreas specimens, including non-involved pancreas tissue adjacent to a duodenal adenoma (1196, (patient ID)), ampullary carcinoma (1258), insulinoma (19–700), and non-involved pancreas tissue adjacent to PDA (1172, 19–262, 19–561, 19–732, 1252), all obtained surgically (**Fig. S1A**). PDA samples were collected from either surgical (n=7) or fine needle biopsy (FNB) (n=3) procedures, and clinical annotation is shown in **Fig. S1A**. Human patient tissues from FNB or surgery were immediately placed into DMEM media supplemented with Y27632 (Rho-Kinase inhibitor) for transport to the laboratory. Sample Preparation, Analysis and Data analysis are described in detail in the Online Methods.

Immunofluorescent staining

Patient tissue slides were rehydrated in xylene, 100% ethanol, 95% ethanol, then running deionized water sequentially. Antigen retrieval was performed with sodium citrate, pH 6.0. Tissue was blocked in 10% donkey serum overnight at 4°C. Primary antibodies (PVR/CD155 (1:100, Cell Signaling Technology), VE-Cadherin/CD144 (1:250, R&D), FOXP3 (1:100, Cell Signaling), Vimentin (1:100, Cell Signaling), CD163 (1:100, Novus Biologicals), or Pan Cytokeratin-488 (1:250, Thermo Fisher Scientific) were diluted in 5% donkey serum in PBST (DS/PBST) and incubated overnight at 4°C. For tissue co-stained for TIGIT-FOXP3 and PVR-Vimentin: the tyramide signal amplification kit with Alexa Fluor 488 (Thermo Fisher Scientific) was used following the manufacturer's recommendation to enhance signaling for PVR and FOXP3. Samples underwent a second citrate antigen retrieval and were then multiplexed with TIGIT and Vimentin following the aforementioned standard IFC protocol. A 1% BSA block was used throughout the TSA protocol and subsequent multiplex staining. Tissue was mounted with DAPI ProLong™ Gold Antifade Mountant (Thermo Fisher Scientific) and subsequently imaged by confocal microscopy on a Leica SP5. Supplementary Table 4 lists the antibodies used.

Statistical Analysis and Reproducibility

Significance was evaluated by the following statistical analyses: two-tailed, parametric, unpaired Student's *t*-test, Student's *t*-test with Welch's correction, Wilcoxon rank-sum test, or a Mann–Whitney *U*-test in GraphPad Prism (version 7) or JMP Pro software (version 14). The data were presented as means ± standard error (SEM) or means ± standard deviation (STDV). A p value of $p<0.05$ was considered statistically significant. Pearson correlation coefficients were used to measure R and R^2. Intergroup comparisons (differential expression) of scRNA seq was performed using Wilcoxon ranked test and p-values were

adjusted for multiple comparisons with the Bonferroni correction method. For the interactome analysis, differences of the ligand and receptors between groups were determined using Wilcoxon ranked test, and p-values were adjusted for multiple comparisons with the Bonferroni correction method. Ligand/Receptor pairs were considered significantly different if the $p < 1.0\times10^{-4}$. Ligand/Receptor pairs were then sorted by the adjusted ligand expression p-value. No statistical method was used to predetermine sample sizes, experiments were not randomized and mass cytometric analysis of samples was not blinded. No data were excluded from the analyses. Each patient is considered an independent biological sample in the analyses. For comparison of differential abundance analysis of mass cytometry data, the edegR package (version 3.11) was used.

Additional Experimental procedures are included in the Online Methods.

Data Availability

All raw data are publicly available without restrictions. All mass cytometry data used for this publication have been deposited in the FlowRepository. All fcs files of tissue (tumor and adjacent normal) have been uploaded to FlowRepository Experiment FR-FCM-Z2S4 and PBMC files have been uploaded to FlowRepository Experiment FR-FCM-Z2S3. The corresponding file key for the FCS files is in supplementary table 6 and refers to Figures 1 and 7, and Extended Data 6 and 7. Single cell RNA sequencing data with clinical metadata are available at NIH dbGAP database under the accession phs002071.v1.p1. Deidentified single cell RNA sequencing data are available at NIH GEO database under the accession GSE155698. Source data are available for this study. All other data supporting the findings of this study are available from the corresponding author on reasonable request.

Code Availability

Code is publicly available on GitHub.com (https://github.com/PascaDiMagliano-Lab/MultimodalMappingPDA-scRNASeq).

Online Methods

Multiplex fluorescent immunohistochemistry (mfIHC) imaging, cell segmentation, and basic phenotyping

Images were taken using the Mantra™ Quantitative Pathology Work Station (Akoya Biosciences) as described in the Online Methods. One image was taken of each patient core. All cube filters were used for each image capture (DAPI, CY3, CY5, CY7, Texas Red, Qdot) and the saturation protection feature was utilized. After all images were acquired, images were analyzed using inForm® Cell Analysis™ software versions 2.3.0 and 2.4.2 (Akoya Biosciences). Using this software, chronic pancreatitis specimens and PDA specimens were batch analyzed by their separate diagnoses. Cell segmentation was completed using DAPI as a basis of cell location and size and all cells segmented into the following subsets (nucleus, cytoplasm, and membrane). Using the automated training software, basic phenotypes (T cells, tumor epithelial cells, other cells, $CD163^+$ cells) were created. Software output consisting of mean fluorescent intensity (mfi) of each antibody-fluorophore pair, basic phenotypes, and x and y coordinates were acquired for further processing. A total of 34

chronic pancreatitis patients and 71 PDA patients were included in this study. Supplemental Table 3 details the antibodies used for mfIHC.

Cytometry Time-of-Flight (CyTOF) Immune Phenotyping

Tissues were mechanically minced and enzymatically digested with collagenase P (1mg/mL DMEM) at 37 degrees Celsius with gentle shaking and subsequently filtered through a 40μm mesh to obtain single cells. Whole blood was collected pre-operatively into two 10mL EDTA tubes. EDTA tubes were inverted 10 times before centrifugation at room temperature (RT), 1700 × g for 20 minutes. Serum was removed and using a P1000 tip, the white layer of PBMCs at the interface between serum and RBCs was removed and placed into 15mL falcon tube. PBMCs were washed in 3X volume PBS centrifuged at RT, 300 × g for 15 minutes. Following centrifugation, the supernatant was removed, and 10ml ACK lysis buffer was added to lyse RBCs for 10 minutes at RT. Following this, PBMCs were centrifuged at 300 × g for 5 minutes. PBMC and tissue samples were washed twice with MaxPar® PBS (Fluidigm) prior to Cell-ID™ Cisplatin (Live/Dead staining). Cell-ID™ Cisplatin reagent (1.67μM) was incubated with tissue and PBMCs single cell suspensions for 5 minutes at RT. To quench this reaction, 4mL of Cell Staining Buffer (Fluidigm) was added to each sample and samples were centrifuged at 300 g for 5 minutes. The supernatant was removed, and cells were washed with 2 mL of MaxPar® Cell Staining Buffer. Cell fixation was achieved by removing the supernatant, and re-suspending the cell pellet in residual volume, prior to the addition of freshly prepared cell fixation buffer (1.6% Methanol-free Formaldehyde; Thermo Fisher 28906 in MaxPar® PBS) for 10 minutes at RT. After fixation, samples were washed twice with 2mL of MaxPar® Cell Staining Buffer and centrifuged at 300 g for 5 minutes. Samples were re-suspended in 1mL MaxPar® Cell Staining Buffer and stored at 4 degrees Celsius for up to one week prior to staining. Up to 3 million cells per sample were stained with cell surface antibody cocktail (All antibodies were purchased from Fluidigm and used at the following dilutions: (CD3 (1:200); CD19 (1:300); CD15 (1:400); CD163 (1:100); CD64 (1:100); CD16 (1:400); LAMP1 (1:100); CD66b (1:200); CCR2 (1:200); TIGIT (1:100); PD-1 (1:100); PD-L1 (1:100); CD8a (1:200); CD33 (1:200); CD45RO (1:200); CD34 (1:100); CD45RA (1:100); CD206 (1:100); CD25 (1:100); CTLA-4 (1:100); CD68 (1:100); PD-L2 (1:100); HLA-DR (1:400); CD14 (1:100); CD4 (1:100); CD11b (1:200); CD45 (1:200); LAG3 (1:100); CD23 (1:100); CD56 (1:100)). (see Supplemental Table 1 for additional antibody information) in 100μl volume of MaxPar® Cell Staining Buffer for 30 minutes at room temperature. After being washed once in 1mL MaxPar® Cell Staining Buffer cells were re-suspended in 2mL cell intercalation solution (125 nM Cell-ID Intercalator-Ir in MaxPar® Fix and Perm Buffer) and shipped to either the Flow Cytometry core at the University of Rochester Medical Center or the Indiana University Simon Cancer Center Flow Cytometry where CyTOF2 Mass Cytometer cell acquisition was performed.

CyTOF Data Preprocessing

Normalized FCS files were analyzed using the Premium CytoBank Software V7.3.0 (cytobank.org). Data were checked for quality of staining and normalized by the use of internal bead standards. Live singlet cells were identified using the combination of Ir191 DNA Intercalator, Event Length, and Pt195 Cisplatin staining intensity channels. Filtered live single cells were exported as new FCS files for downstream analysis.

CyTOF Analysis

Unbiased identification of cellular subpopulations was performed in parallel using multiple approaches – visualization through FlowSOM-viSNE in R, where an initial FlowSOM clustered cells into 100 initial nodes, followed by the ConsensusClusterPlus package which, along with manual annotation helped to further consolidate the clusters based on cell surface marker expression [18], or Astrolabe Cytometry Platform (Astrolabe Diagnostics, Inc.), where single-cell data was clustered using the FlowSOM R package [61] and labeled using the Ek'Balam algorithm [19]. The hierarchical clustering for all heatmaps uses the Pearson's correlation as a distance metric. Differential abundance analysis was performed using the edgeR V3.11 R package [62, 63]. We used a combination of manual gating validation and unbiased approaches to analyze our datasets and included samples with >3000 live singlets in clustering algorithms.

Treatment of Batch Effects

In order to avoid batch effects within the data analysis, the Astrolabe Cytometry Platform did not compare numerical intensities between samples [19]. Each sample was analyzed separately, and then comparisons were done using either cell frequencies (such as comparing T Cell counts) or qualitative values ("CD3 high" versus "CD3 low"). The underlying assumption was that a given subset was the same regardless of if underlying marker intensity has shifted; in other words, a T Cell was defined as a T Cell whether the $CD3^+$ peak was centered around a transformed intensity of 4, or a transformed intensity of 6. This mirrors the approach utilized in manual gating analysis.

t-SNE Visualization

For the t-SNE maps, each sample was uniformly downsampled into at most 10,000 cells. Samples were then concatenated, and the complete data set was uniformly downsampled into at most 500,000 cells. t-SNE algorithm was run using the Rt-SNE package: https://github.com/jkrijthe/Rt-SN.

Single-cell RNA sequencing

Tissues were mechanically minced and enzymatically digested with collagenase P (1mg/mL DMEM) and subsequently filtered through a 40μm mesh to obtain single cells. Dead cells were removed using MACS® Dead Cell Removal Kit (Miltenyi Biotec Inc.). Single-cell cDNA libraries were prepared and sequenced at the University of Michigan Sequencing Core using the 10x Genomics Platform. Samples were run using paired end 50 cycle reads on HiSeq 4000 or the NovaSeq 6000 (Illumina) to a depth of 100,000 reads. The raw data were processed and aligned by the University of Michigan DNA Sequencing Core. Cellranger count version 3.0.0 with default settings was used, with an initial expected cell count of 10,000. In all cases the hg19 reference supplied with the cellranger software was used for alignment. R Studio V3.5.1 and R package Seurat version 3.0 was used for single cell RNA-seq data analysis similarly as previous described. Data were initially filtered to only include all cells with at least 200 genes and all genes in greater than 3 cells. Data were initially normalized using the NormalizeData function with a scale factor of 10,000 and the LogNormalize normalization method. Variable genes were identified using the

FindVariableFeatures function. Data were assigned a cell cycle score using the CellCycleScoring function and a cell cycle difference was calculated by subtracting the S phase score from the G2M score. Data were scaled and centered using linear regression on the counts and the cell cycle score difference. PCA was run with the RunPCA function using the previously defined variable genes. Violin plots were then used to filter data according to user-defined criteria. All tissue samples were batch corrected through the R package Harmony V1.0 (https://github.com/immunogenomics/harmony). Harmony is a flexible multi-dataset integration algorithm for scRNA-seq by correcting the low-dimensional embedding of cells from principal component analysis (PCA). It first uses soft clustering to find potential clusters, and then uses a soft k-means clustering algorithm to find clusters that favors the cells from multiple datasets and penalizes for any specified unwanted technical or biological factors. It then learns a simple linear adjustment function by computing cluster-specific linear correction factors, such as individual cell-types and cell state, from the cluster-specific centroids from each dataset. Each cell is weighted and corrected by its cell-specific linear factor. It then iterates the clustering and correction until the cell cluster assignments are stable. We used Harmony V1.0 to integrate our scRNA-seq patient data, correcting for individual scRNA-seq Run IDs (as each individual patient was each their own Run ID). Cell clusters were identified via the FindNeighbors and FindClusters function using a resolution of 1.2–2 for all samples and Uniform Manifold Approximation and Projection (UMAP) clustering algorithms were performed. FindAllMarkers table was created and clusters were defined by user-defined criteria. Code is publicly available on GitHub.com (https://github.com/PascaDiMagliano-Lab/MultimodalMappingPDA-scRNASeq).

Interactome

Ligand and receptor pairs were defined based off of a curated literature supported list in Ramilowski et al [50]. The average of expression of ligands and receptors (LR) in all the population for each group were calculated. LR pairs in each group (adjacent/normal and PDA) were determined to be expressed by setting the median average expression for all groups as a threshold. LR's above the threshold were considered as expressed in the group. LR pairs were then filtered out if the ligand and receptor in the LR pairs were not expressed in both groups. Differences of the LR's between groups were determined using Wilcoxon ranked test, and p-values were adjusted for multiple comparisons with the Bonferroni correction method. LR's were considered significantly different if the $p < 1.0\times10^{-4}$. LR pairs were then sorted by the adjusted ligand expression p-value. The interactomes were visualized using the Circos software V0.69-9 and the heatmap values within the circos plots displays the average expression of each ligand/receptor within the PDA tissues [64].

Extended Data

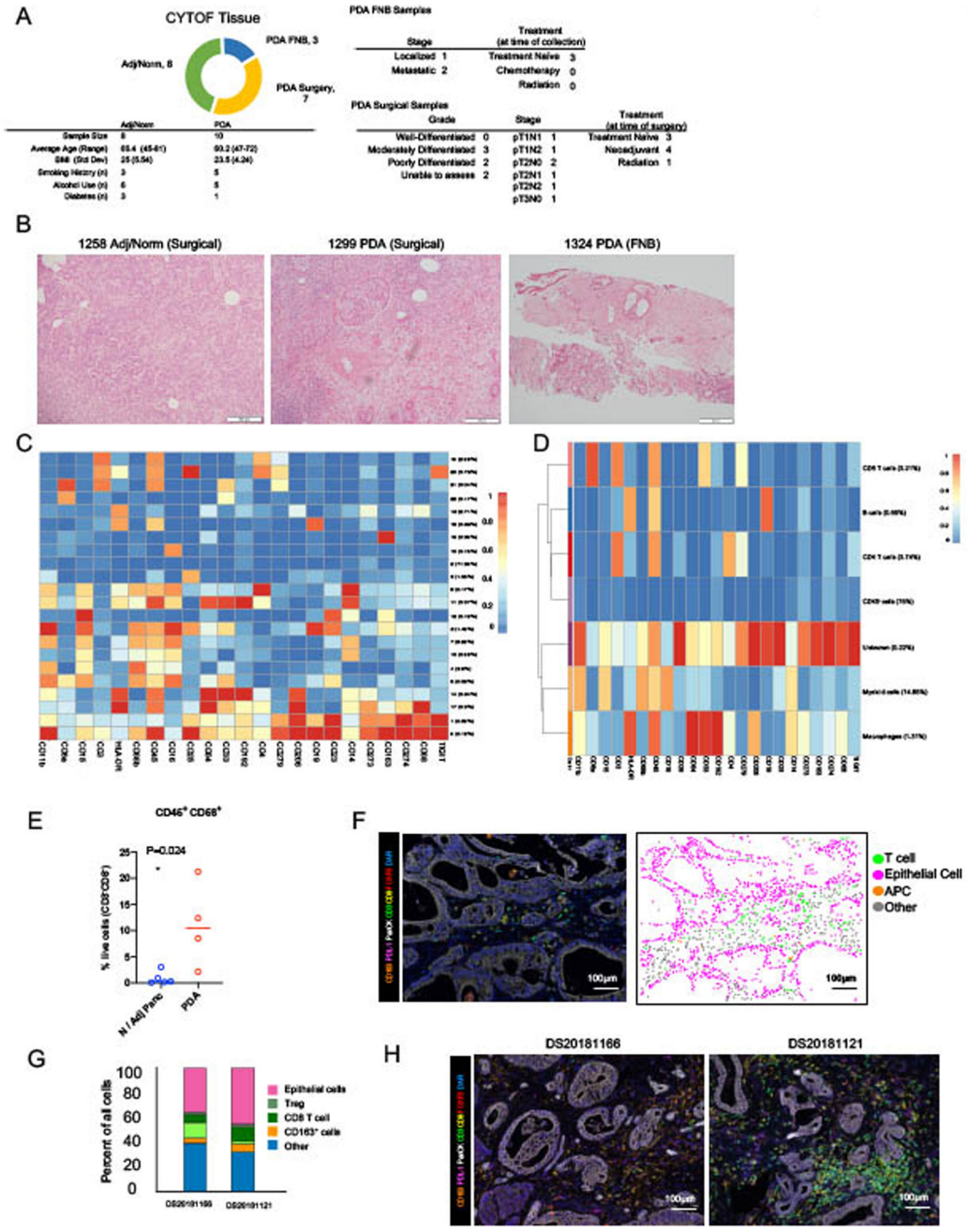

Extended Data Figure 1. CyTOF and multiplex fluorescent immunohistochemistry (mfIHC) mapping can be readily performed on patient tumor samples and show a heterogeneous immune infiltration in human pancreatic cancer.

(A) Patient breakdown and tumor characteristics of CyTOF performed on 8 adj/norm pancreas and 10 PDA tumor samples (surgical (7) vs. fine needle biopsy (FNB) (3)). **(B)** Representative H&E stains of samples DS20191258 (Adj/Norm), DS20191299 (PDA tumor from surgical resection), and DS20191324 (PDA tumor from fine needle biopsy). **(C)** The ConsensusClusterPlus and FlowSOM R packages were used to define the initial 22 clusters

identified in the tissue CyTOF samples. **(D)** Final heatmap demonstrating marker expression used to define cell populations. **(E)** Manual gating of CD3-CD8A-CD45+CD56+ NK cells in adjacent/normal and PDA tissue samples, n=5 adjacent/normal tissue samples and n=4 PDA tissue samples. Two-sided Student's *t*-test was performed to compare between groups and asterisk indicates a p value of less than 0.05 was considered significant. For manual gating of NK cells n=5 for adj/norm and n=4 for PDA patient samples. **(F)** mfIHC composite image of PDA (left). Phenotype map with the following basic phenotypes at their x and y coordinates: T cell (green), epithelial cells (pink), APCs (orange), other cells (grey) (right). 71 individual PDA and 34 individual chronic pancreatitis subjects were examined in this analysis. **(G)** Relative cellular composition by quantitation of mfIHC of representative surgical PDA tissue of additional patients DS20181166 (PDA tumor from distal pancreatectomy), DS20181141 (PDA tumor from distal pancreatectomy) **(H)** Corresponding mfIHC images of DS20181166, and DS20181141.

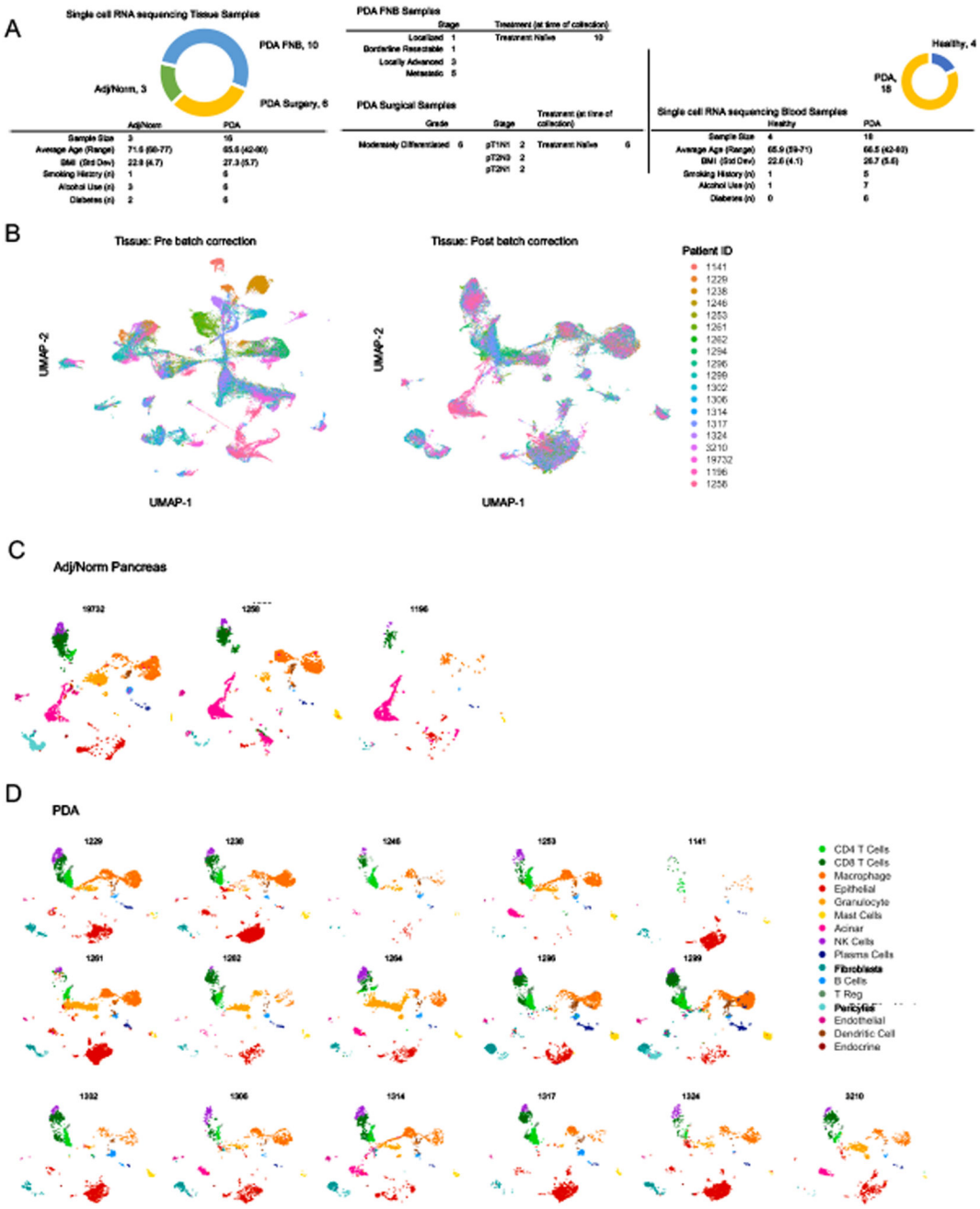

Extended Data Figure 2. Single Cell RNA Sequencing of PDA tissue reveals heterogeneous cellular composition and expression of immune checkpoints.

(A) Single cell RNA sequencing tissue sample breakdown (n = 3 Adj/Norm tissue, n=10 PDA tissue from fine needle biopsy, and n=6 PDA tissue from surgical resection), patient clinical data, and tumor characteristics (grade and stage) (Left panel). Breakdown of sequenced PBMC samples with corresponding patient clinical data (Right panel). (**B**) UMAP of the merged tissue colored by Patient ID prior to batch correction (Left panel) and post batch correction (Right panel). **(C)** UMAP of 3 individual adjacent/normal samples and **(D)** 16 PDA tissues. We distinguished two epithelial populations: tumor cells and acinar

cells. In the non-epithelial compartment, we identified fibroblasts, pericytes, $CD8^+$ T cells, $CD4^+$ T cells, Tregs, NK cells, B cells, plasma cells, mast cells, macrophages, granulocytes, dendritic cells, endothelial cells, and a small endocrine population.

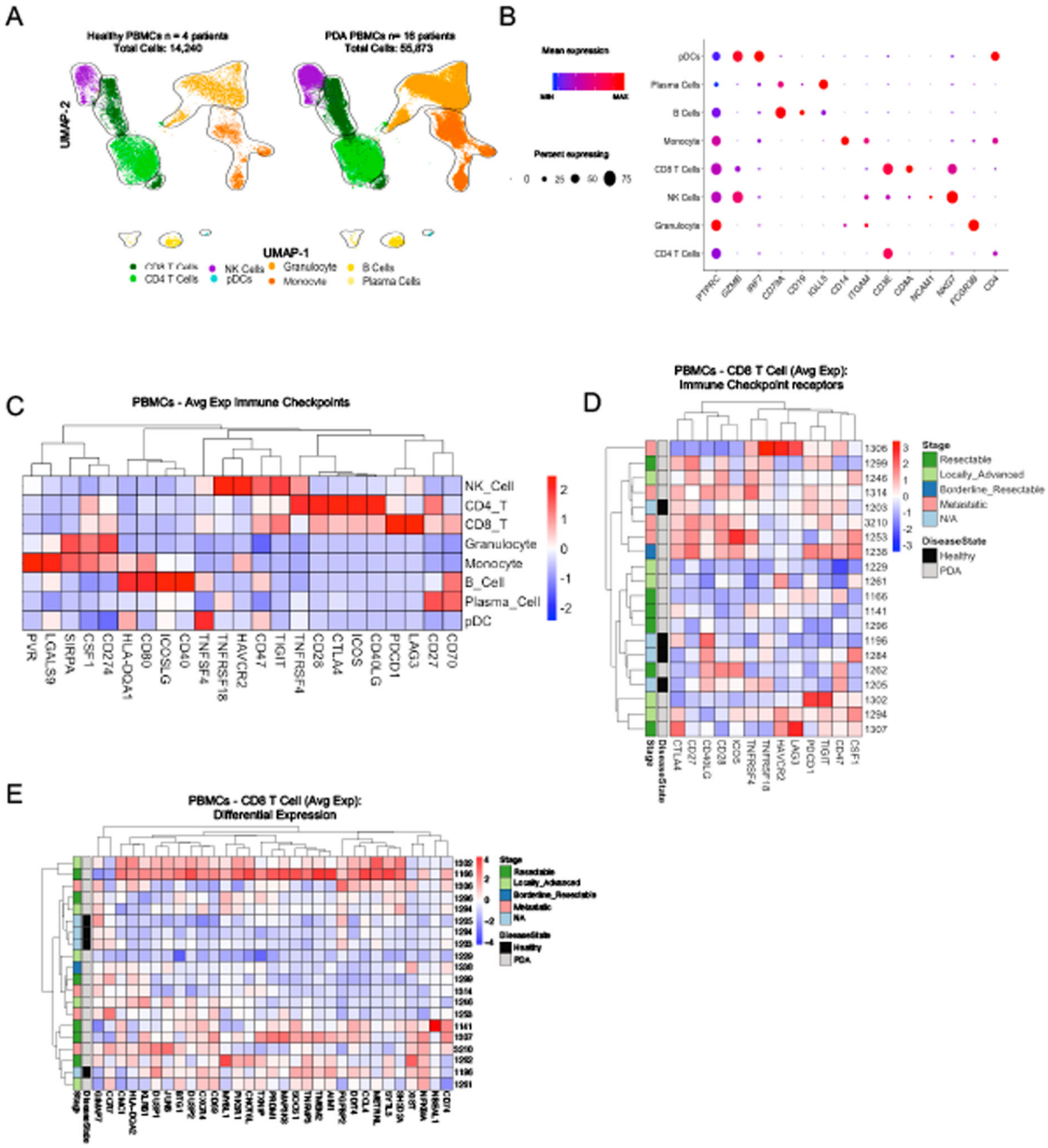

Extended Data Figure 3. Single Cell RNA Sequencing of PDA PBMCs reveals heterogeneous cellular composition and expression of immune checkpoints.

(A) Merged UMAP plots of PBMCs from 4 healthy donors and 16 PDA patients (total of 70,113 cells). CD8 T cells (green), CD4 T cells (light green), NK cells (purple), pDCs (blue), Granulocyte (light orange), Monocyte (orange), B cells (yellow), Plasma cells (light yellow). (**B)** Dot plot analysis of key markers to define the 8 identified cell populations.

Color of dot represents average expression, while the size of the dot represents percent expression. Dot plot represents merged healthy (n=4) and PDA (n=16) patient gene expression of PBMC lineage markers. **(C)** Average expression of immune checkpoint ligands and receptors in the identified cell populations in merged blood samples. **(D)** Average expression of immune checkpoint receptors on CD8$^+$ T cells in merged PBMCs. **(E)** Average expression of differentially expressed genes in CD8$^+$ T cells comparing healthy (black) to PDA (grey) PBMCs. Disease stage is plotted on the left.

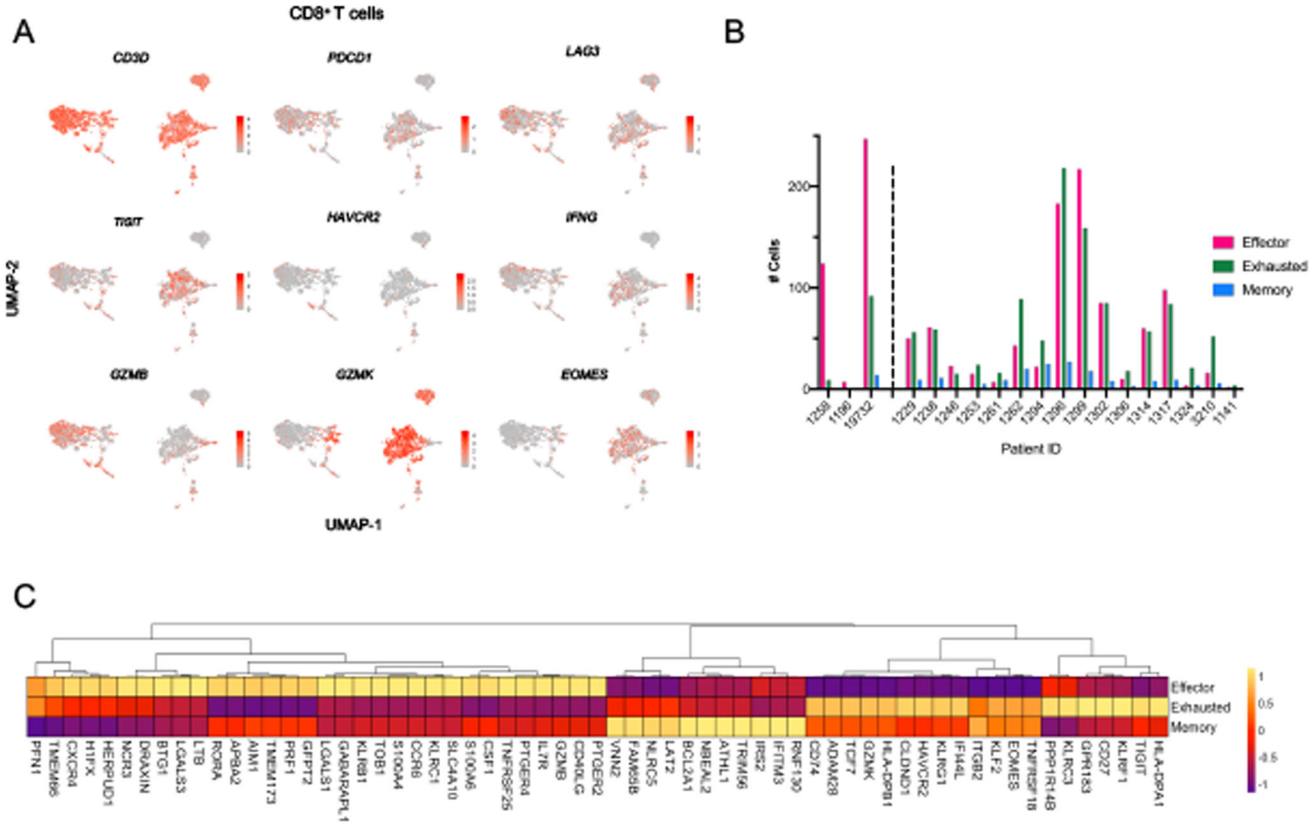

Extended Data Figure 4. Single cell RNA sequencing reveals 3 CD8$^+$ T cell populations: effector, exhausted, and memory CD8$^+$ T Cells.

(A) Feature plots of immune checkpoints (*PDCD1, LAG3, TIGIT, HAVCR2)*, activation markers (*IFNG, GZMB)*, and exhaustion markers *(GZMK, EOMES)* in CD8$^+$ T cells. **(B)** Number of effector (pink), exhausted (green), and memory (blue) CD8$^+$ T cells captured in each individual tissue sample by scRNA seq. **(C)** Average scaled expression heatmap of highly enriched genes by potential effector, exhausted, and memory cell populations. (n = 3 Adj/Norm tissue and n= 16 PDA tissue for panels A–C).

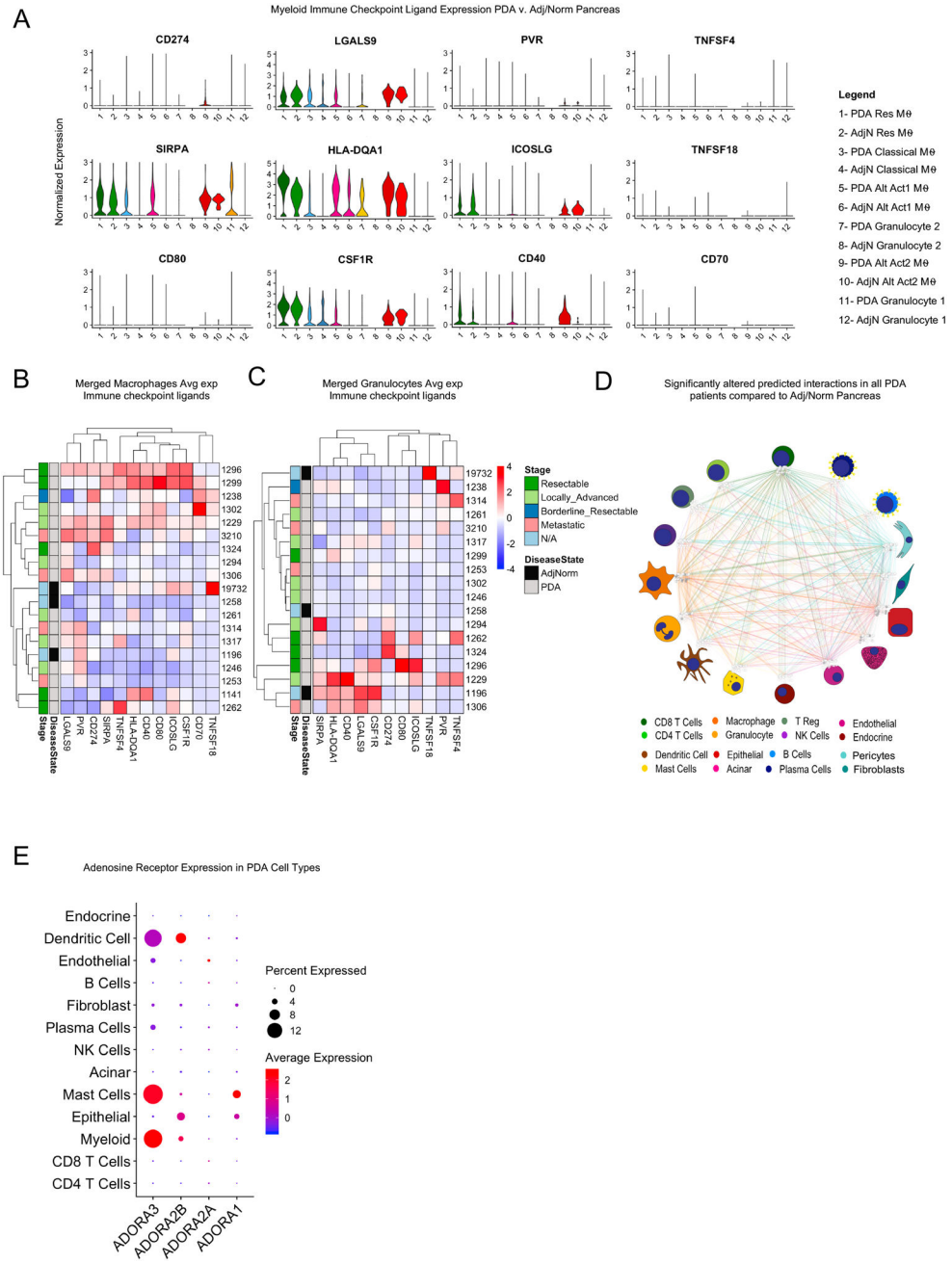

Extended Data Figure 5. Single cell RNA sequencing of myeloid subsets in human pancreatic cancer.

(A) Violin Plots illustrating comparison of immune checkpoint ligands in myeloid clusters in PDA vs. adjacent normal/pancreas samples. **(B)** Average expression heatmap of checkpoint ligands in merged macrophages (all cells expressing *CD68* within the myeloid population) and **(C)** merged granulocytes (all cells expressing *FCGR3B* within the myeloid population). Left panels denote disease state (adjacent/normal vs. PDA tissue) and stage. **(D)** Map of all putative ligand receptor differential interactions that are upregulated in 16 PDA compared to 3 adjacent/normal pancreas. The line color denotes cellular source of the ligand, and putative

interactions were visualized in Cytoscape® V3.7.1. **(E)** Dot plot analysis showing expression of adenosine receptors in PDA tumor cell types. Red indicates high expression, blue low expression, and the size of the dot is relative to the percent that marker is expressed. Dot plot represent n=16 PDA patient gene expression of adenosine receptors.

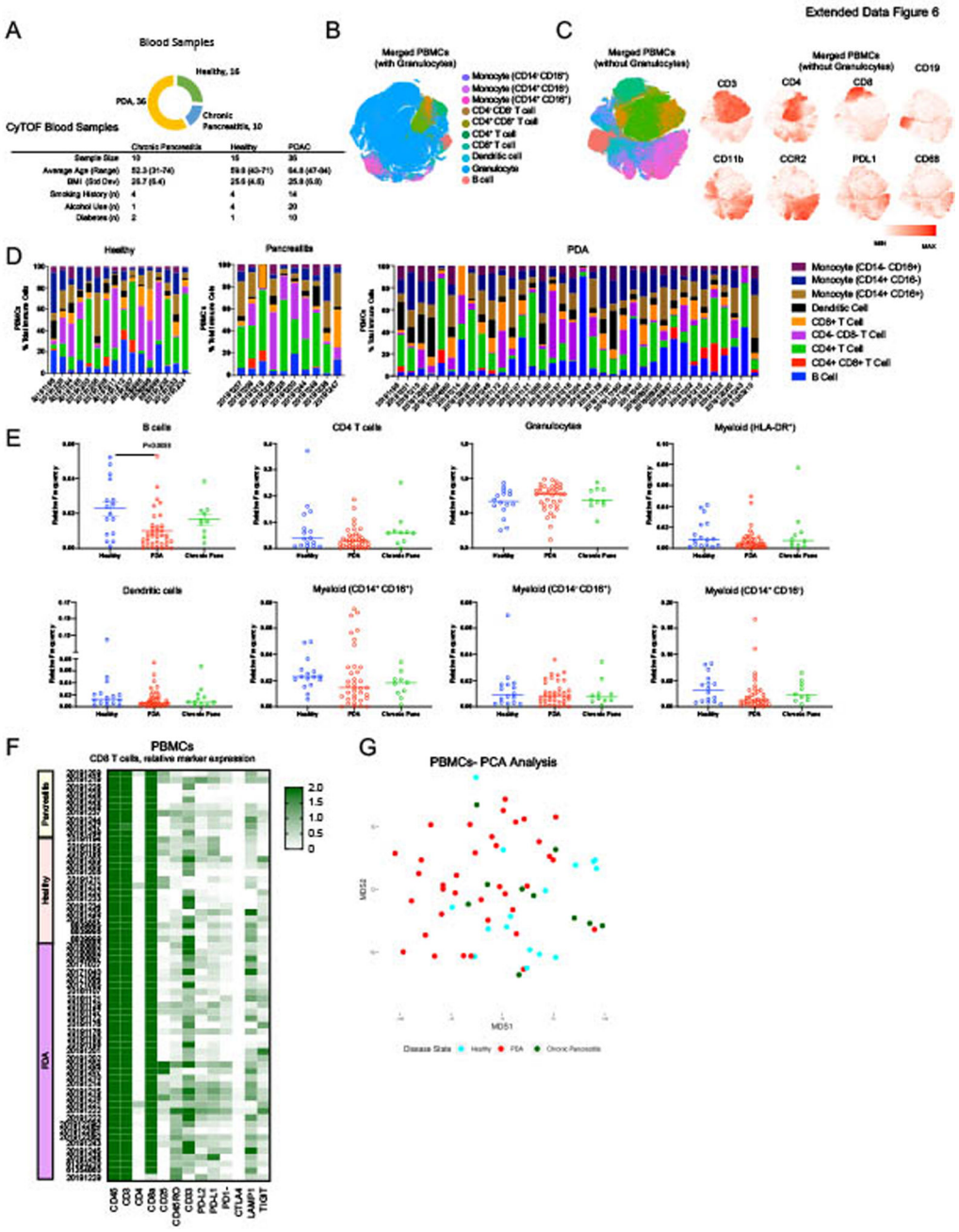

Extended Data Figure 6. CyTOF analysis of PBMCs from healthy, chronic pancreatitis, and PDA patients.

(A) Patient breakdown and characteristics of CyTOF performed on patient blood samples (n = 16 healthy patients, n = 10 chronic pancreatitis patients, and n=36 PDA patients). **(B)** t-SNE analysis of CyTOF of all merged PBMC samples with granulocytes ($CD66b^{+}$). **(C)** t-

SNE analysis of CyTOF of all merged PBMC samples without granulocytes. Key marker t-SNE feature plots of CD3 (total T cells), CD4 (Helper $CD4^+$ T cells), CD8 (Cytotoxic T cells), CD19 (B cells), CD11b (Myeloid cells), CCR2, PDL-1, and CD68 (Macrophage marker). **(D)** Bar plots of relative cell type abundance (B cell, $CD4^+/CD8^+$ T cell, $CD4^+$ T cell, $CD4^-/CD8^-$ T cell, Dendritic cell, $CD14^+/CD16^+$ Monocyte, $CD14^+/CD16^-$ Monocyte, and $CD14^-$ $CD16^+$ Monocyte) from CyTOF of PBMCs of healthy, chronic pancreatitis, and PDA patients. **(E)** Quantification of unbiased analysis (Astrolabe pipeline) of PBMC immune populations in n=16 healthy patients, n=36 PDA patients, and n=10 chronic pancreatitis patients. Two-sided Student's *t*-tests were performed to compare between groups and a p value of <0.05 was considered significant. **(F)** Relative CyTOF marker expression in $CD8^+$ T Cells from PDA tumor tissue. **(G)** PCA analysis of PBMCs at different disease states. Healthy (neon blue), PDA (red), and Chronic Pancreatitis (green).

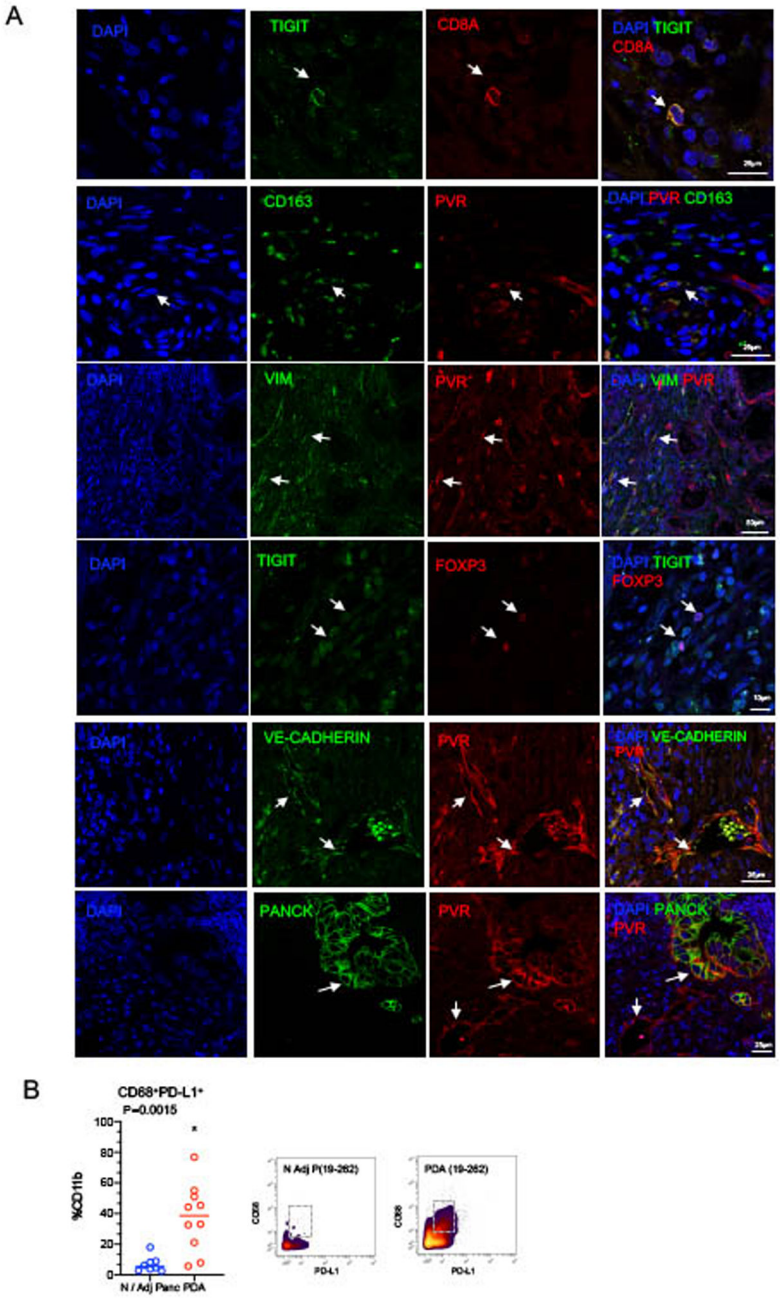

Extended Data Figure 7. Immunofluorescence of immune checkpoints in pancreatic tumors. **(A)** Individual channels of immunofluorescent staining of patient tissues with antibodies specific for TIGIT/CD8A, TIGIT/FOXP3, PVR/Pan-cytokeratin, PVR/CD163, PVR/Vimentin, and PVR/VE-cadherin. Three individual patient tumors were examined independently per staining analysis**. (B)** Manual gating of PD-L1^{+} CD68^{+} macrophages in normal adjacent (n=8) and PDA (n=10) tissue. Two-sided Student's *t*-test was performed, and asterisk indicates a p value of <0.05 was considered statistically significant. Representative individual CyTOF biaxial density plots from normal adjacent and PDA tissue

of a matched patient (19–262) of PD-L1 expression in $CD68^+$ macrophages (as a percentage of total $CD11b^+$ cells).

Supplementary Material

Refer to Web version on PubMed Central for supplementary material.

Acknowledgments:

We thank Matthew Cochran and Terry Wightman at the Flow Cytometry core at the University of Rochester Medical Center and Andrea Michelle Gunawan at the Indiana University Simon Cancer Center Flow Cytometry for their support in cell CyTOF acquisition. We thank Vinicius Motta and Kevin Brown from Fluidigm for their assistance with panel design. We would like to thank Patricia Schnepp and Aquila Ahmed for their assistance with CyTOF experimental design. We would also like to thank Tricia Tamsen and Judy Opp from the University of Michigan Advanced Genomics Core. We would like to thank David Hill and Michael Czerwinski for their input on designing single cell analysis pipelines. We would very much like to thank Amir Gilado and Ido Amit for their expertise in building our pancreatic interactome network. We would like to thank the Tissue Procurement Center at the University of Michigan. Thanks to Ed Stack formerly with Perkin Elmer for assistance with initial R introduction and basic training using inForm 2.3.0 and earlier versions. and staining strategies. We thank Philip Turncliff for the excellent graphics. We also thank Jason Spence for the VE-cadherin antibody gift.

Funding:

This project was supported by NIH/NCI grants R01CA151588, R01CA198074, U01CA224145, and the American Cancer Society to MPdM. This work was also supported by the University of Michigan Cancer Center Support Grant (P30CA046592), including an Administrative Supplement to HCC and MPdM. FB was funded by the Association of Academic Surgery Joel Roslyn Award. TLF was funded by K08CA201581. SK was supported by T32-GM113900 and NS, VS, KD were supported by T32-CA009676. EC is supported the American College of Gastroenterology Clinical Research Award and by T32-DK094775. NS is a recipient of the American Cancer Society Postdoctoral Award PF-19-096-01 and the Michigan Institute for Clinical and Healthy Research (MICHR) Postdoctoral Translational Scholar Program fellowship award. AR and ST were supported by institutional startup funds from the University of Michigan, a gift from Agilent Technologies, NCI grant R37CA214955 and a Research Scholar Grant from the American Cancer Society (RSG-16-005-01). The funders had no role in study design, data collection and analysis, decision to publish, or preparation of the manuscript.

References and Notes:

RStudio Team (2015). RStudio: Integrated Development for R. RStudio, Inc, Boston, MA URL http://www.rstudio.com/.

R Core Team (2017). R: A language and environment for statistical computing. R Foundation for Statistical Computing, Vienna, Austria. URL https://www.R-project.org/.

References:

1. Royal RE, et al., Phase 2 trial of single agent Ipilimumab (anti-CTLA-4) for locally advanced or metastatic pancreatic adenocarcinoma. J Immunother, 2010. 33(8): p. 828–33. [PubMed: 20842054]
2. Brahmer JR, et al., Safety and activity of anti-PD-L1 antibody in patients with advanced cancer. N Engl J Med, 2012. 366(26): p. 2455–65. [PubMed: 22658128]
3. Stromnes IM, et al., T-cell Localization, Activation, and Clonal Expansion in Human Pancreatic Ductal Adenocarcinoma. Cancer Immunol Res, 2017. 5(11): p. 978–991. [PubMed: 29066497]
4. Balli D, et al., Immune Cytolytic Activity Stratifies Molecular Subsets of Human Pancreatic Cancer. Clin Cancer Res, 2017. 23(12): p. 3129–3138. [PubMed: 28007776]
5. Carstens JL, et al., Spatial computation of intratumoral T cells correlates with survival of patients with pancreatic cancer. Nat Commun, 2017. **8**: p. 15095. [PubMed: 28447602] **8**
6. Balachandran VP, et al., Identification of unique neoantigen qualities in long-term survivors of pancreatic cancer. Nature, 2017. 551(7681): p. 512–516. [PubMed: 29132146]

7. Tsujikawa T, et al., Quantitative Multiplex Immunohistochemistry Reveals Myeloid-Inflamed Tumor-Immune Complexity Associated with Poor Prognosis. Cell Rep, 2017. 19(1): p. 203–217. [PubMed: 28380359]
8. Vonderheide RH, The Immune Revolution: A Case for Priming, Not Checkpoint. Cancer Cell, 2018. 33(4): p. 563–569. [PubMed: 29634944]
9. Clark CE, et al., Dynamics of the immune reaction to pancreatic cancer from inception to invasion. Cancer Res, 2007. 67(19): p. 9518–27. [PubMed: 17909062]
10. Moncada R, et al., Integrating microarray-based spatial transcriptomics and single-cell RNA-seq reveals tissue architecture in pancreatic ductal adenocarcinomas. Nat Biotechnol, 2020.
11. Chan-Seng-Yue M, et al., Transcription phenotypes of pancreatic cancer are driven by genomic events during tumor evolution. 2020.
12. Elyada E, et al., Cross-species single-cell analysis of pancreatic ductal adenocarcinoma reveals antigen-presenting cancer-associated fibroblasts. Cancer Discov, 2019.
13. Dominguez CX, et al., Single-cell RNA sequencing reveals stromal evolution into LRRC15+ myofibroblasts as a determinant of patient response to cancer immunotherapy. Cancer Discov, 2019.
14. Manieri NA, Chiang EY, and Grogan JL, TIGIT: A Key Inhibitor of the Cancer Immunity Cycle. Trends Immunol, 2017. 38(1): p. 20–28. [PubMed: 27793572]
15. Cohen M, et al., Lung Single-Cell Signaling Interaction Map Reveals Basophil Role in Macrophage Imprinting. Cell, 2018. 175(4): p. 1031–1044 e18. [PubMed: 30318149]
16. Zhang Q, et al., Landscape and Dynamics of Single Immune Cells in Hepatocellular Carcinoma. Cell, 2019. 179(4): p. 829–845 e20. [PubMed: 31675496]
17. Bendall SC, et al., Single-cell mass cytometry of differential immune and drug responses across a human hematopoietic continuum. Science, 2011. 332(6030): p. 687–96. [PubMed: 21551058]
18. Nowicka M, et al., CyTOF workflow: differential discovery in high-throughput high-dimensional cytometry datasets. F1000Res, 2017. 6: p. 748. [PubMed: 28663787]
19. Amir ED, et al., Development of a Comprehensive Antibody Staining Database Using a Standardized Analytics Pipeline. Front Immunol, 2019. 10: p. 1315. [PubMed: 31244854]
20. Zhang Y, et al., Myeloid cells are required for PD-1/PD-L1 checkpoint activation and the establishment of an immunosuppressive environment in pancreatic cancer. Gut, 2017. 66(1): p. 124–136. [PubMed: 27402485]
21. Panni RZ, et al., Agonism of CD11b reprograms innate immunity to sensitize pancreatic cancer to immunotherapies. Sci Transl Med, 2019. 11(499).
22. Stromnes IM, et al., Targeted depletion of an MDSC subset unmasks pancreatic ductal adenocarcinoma to adaptive immunity. Gut, 2014. 63(11): p. 1769–81. [PubMed: 24555999]
23. Lazarus J, et al., Spatial and phenotypic immune profiling of metastatic colon cancer. JCI Insight, 2018. 3(22).
24. Beatty GL, et al., Exclusion of T Cells From Pancreatic Carcinomas in Mice Is Regulated by Ly6C(low) F4/80(+) Extratumoral Macrophages. Gastroenterology, 2015. 149(1): p. 201–10. [PubMed: 25888329]
25. Sanford DE, et al., Inflammatory monocyte mobilization decreases patient survival in pancreatic cancer: a role for targeting the CCL2/CCR2 axis. Clin Cancer Res, 2013. 19(13): p. 3404–15. [PubMed: 23653148]
26. DeNardo DG and Ruffell B, Macrophages as regulators of tumour immunity and immunotherapy. Nature Reviews Immunology, 2019. 19(6): p. 369–382.
27. Nywening TM, et al., Targeting both tumour-associated CXCR2(+) neutrophils and CCR2(+) macrophages disrupts myeloid recruitment and improves chemotherapeutic responses in pancreatic ductal adenocarcinoma. Gut, 2018. 67(6): p. 1112–1123. [PubMed: 29196437]
28. Zhu Y, et al., Tissue-Resident Macrophages in Pancreatic Ductal Adenocarcinoma Originate from Embryonic Hematopoiesis and Promote Tumor Progression. Immunity, 2017. 47(2): p. 323–338 e6. [PubMed: 28813661]

29. Zhu Y, et al., CSF1/CSF1R blockade reprograms tumor-infiltrating macrophages and improves response to T-cell checkpoint immunotherapy in pancreatic cancer models. Cancer Res, 2014. 74(18): p. 5057–69. [PubMed: 25082815]
30. Rosenberg SA, Decade in review-cancer immunotherapy: entering the mainstream of cancer treatment. Nat Rev Clin Oncol, 2014. 11(11): p. 630–2. [PubMed: 25311350]
31. Carlson CM, et al., Kruppel-like factor 2 regulates thymocyte and T-cell migration. Nature, 2006. 442(7100): p. 299–302. [PubMed: 16855590]
32. Wherry EJ, et al., Molecular signature of CD8+ T cell exhaustion during chronic viral infection. Immunity, 2007. 27(4): p. 670–84. [PubMed: 17950003]
33. Li J, et al., High Levels of Eomes Promote Exhaustion of Anti-tumor CD8(+) T Cells. Front Immunol, 2018. 9: p. 2981. [PubMed: 30619337]
34. Jansen CS, et al., An intra-tumoral niche maintains and differentiates stem-like CD8 T cells. Nature, 2019. 576(7787): p. 465–470. [PubMed: 31827286]
35. Kondo T, Takata H, and Takiguchi M, Functional expression of chemokine receptor CCR6 on human effector memory CD8+ T cells. Eur J Immunol, 2007. 37(1): p. 54–65. [PubMed: 17171755]
36. Ducimetiere L, Vermeer M, and Tugues S, The Interplay Between Innate Lymphoid Cells and the Tumor Microenvironment. Front Immunol, 2019. 10: p. 2895. [PubMed: 31921156]
37. Arlettaz L, et al., Expression of inhibitory KIR is confined to CD8+ effector T cells and limits their proliferative capacity. Eur J Immunol, 2004. 34(12): p. 3413–22. [PubMed: 15549734]
38. McMahon CW, et al., Viral and bacterial infections induce expression of multiple NK cell receptors in responding CD8(+) T cells. J Immunol, 2002. 169(3): p. 1444–52. [PubMed: 12133970]
39. Smith SL, et al., Diversity of peripheral blood human NK cells identified by single-cell RNA sequencing. Blood Adv, 2020. 4(7): p. 1388–1406. [PubMed: 32271902]
40. Zhang Y, et al., CD4+ T lymphocyte ablation prevents pancreatic carcinogenesis in mice. Cancer Immunol Res, 2014. 2(5): p. 423–35. [PubMed: 24795355]
41. Zhang Y, et al., Regulatory T cell depletion alters the tumor microenvironment and accelerates pancreatic carcinogenesis. Cancer Discov, 2020.
42. Jang JE, et al., Crosstalk between Regulatory T Cells and Tumor-Associated Dendritic Cells Negates Anti-tumor Immunity in Pancreatic Cancer. Cell Rep, 2017. 20(3): p. 558–571. [PubMed: 28723561]
43. Sckisel GD, et al., Differential phenotypes of memory CD4 and CD8 T cells in the spleen and peripheral tissues following immunostimulatory therapy. J Immunother Cancer, 2017. **5**: p. 33. [PubMed: 28428882] **5**
44. Bengsch F, et al., CTLA-4/CD80 pathway regulates T cell infiltration into pancreatic cancer. Cancer Immunol Immunother, 2017. 66(12): p. 1609–1617. [PubMed: 28856392]
45. Hegde S, et al., Dendritic Cell Paucity Leads to Dysfunctional Immune Surveillance in Pancreatic Cancer. Cancer Cell, 2020. 37(3): p. 289–307 e9. [PubMed: 32183949]
46. Huber S, et al., IL-22BP is regulated by the inflammasome and modulates tumorigenesis in the intestine. Nature, 2012. 491(7423): p. 259–63. [PubMed: 23075849]
47. Lanfranca MP, et al., Interleukin 22 Signaling Regulates Acinar Cell Plasticity to Promote Pancreatic Tumor Development in Mice. Gastroenterology, 2019.
48. Collin M and Bigley V, Human dendritic cell subsets: an update. Immunology, 2018. 154(1): p. 3–20. [PubMed: 29313948]
49. Veglia F and Gabrilovich DI, Dendritic cells in cancer: the role revisited. Curr Opin Immunol, 2017. 45: p. 43–51. [PubMed: 28192720]
50. Ramilowski JA, et al., A draft network of ligand-receptor-mediated multicellular signalling in human. Nat Commun, 2015. 6: p. 7866. [PubMed: 26198319]
51. Das S, et al., Tumor Cell-Derived IL-1beta Promotes Desmoplasia and Immune Suppression in Pancreatic Cancer. Cancer Res, 2020.
52. Ohlund D, et al., Distinct populations of inflammatory fibroblasts and myofibroblasts in pancreatic cancer. J Exp Med, 2017. 214(3): p. 579–596. [PubMed: 28232471]

53. Fourcade J, et al., CD226 opposes TIGIT to disrupt Tregs in melanoma. JCI Insight, 2018. 3(14).
54. Yu X, et al., The surface protein TIGIT suppresses T cell activation by promoting the generation of mature immunoregulatory dendritic cells. Nat Immunol, 2009. 10(1): p. 48–57. [PubMed: 19011627]
55. Maj T, et al., Oxidative stress controls regulatory T cell apoptosis and suppressor activity and PD-L1-blockade resistance in tumor. Nat Immunol, 2017. 18(12): p. 1332–1341. [PubMed: 29083399]
56. Ligorio M, et al., Stromal Microenvironment Shapes the Intratumoral Architecture of Pancreatic Cancer. Cell, 2019. 178(1): p. 160–175 e27. [PubMed: 31155233]
57. Stuart T and Satija R, Integrative single-cell analysis. Nat Rev Genet, 2019. 20(5): p. 257–272. [PubMed: 30696980]
58. Xu J, et al., Peripheral Blood T-Cell Fitness Is Diminished in Patients With Pancreatic Carcinoma but Can Be Improved With Homeostatic Cytokines. Cell Mol Gastroenterol Hepatol, 2019. 8(4): p. 656–658 e6. [PubMed: 31398492]
59. Zhang Q, et al., Blockade of the checkpoint receptor TIGIT prevents NK cell exhaustion and elicits potent anti-tumor immunity. Nat Immunol, 2018. 19(7): p. 723–732. [PubMed: 29915296]
60. Solomon BL and Garrido-Laguna I, TIGIT: a novel immunotherapy target moving from bench to bedside. Cancer Immunol Immunother, 2018. 67(11): p. 1659–1667. [PubMed: 30232519]
61. Van Gassen S, et al., FlowSOM: Using self-organizing maps for visualization and interpretation of cytometry data. Cytometry Part A, 2015. 87a(7): p. 636–645.
62. McCarthy DJ, Chen Y, and Smyth GK, Differential expression analysis of multifactor RNA-Seq experiments with respect to biological variation. Nucleic Acids Res, 2012. 40(10): p. 4288–97. [PubMed: 22287627]
63. Robinson MD, McCarthy DJ, and Smyth GK, edgeR: a Bioconductor package for differential expression analysis of digital gene expression data. Bioinformatics, 2010. 26(1): p. 139–40. [PubMed: 19910308]
64. Krzywinski M, et al., Circos: an information aesthetic for comparative genomics. Genome Res, 2009. 19(9): p. 1639–45. [PubMed: 19541911]

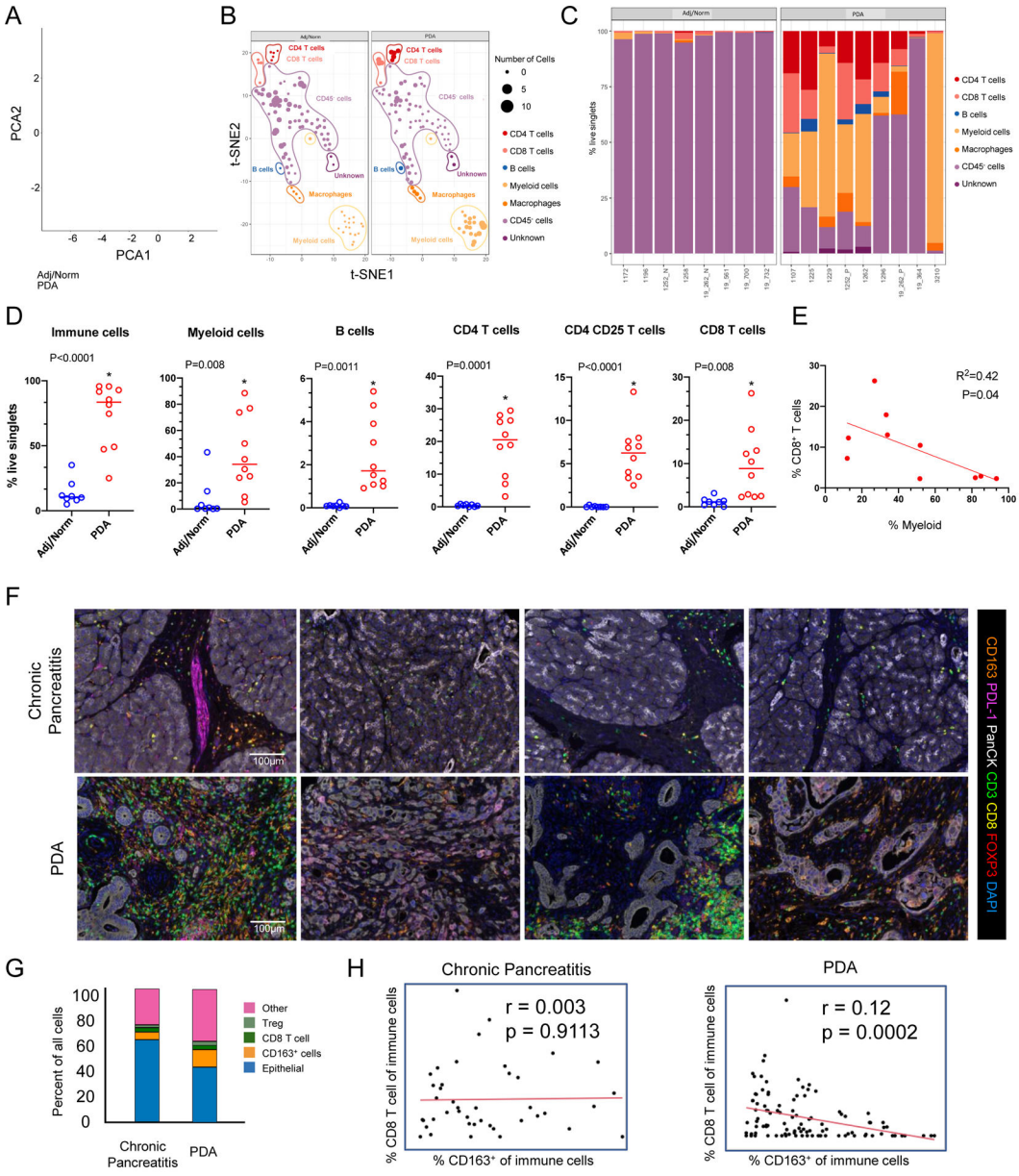

Figure 1. CyTOF and multiplex fluorescent immunohistochemistry (mfIHC) mapping reveals heterogeneous immune infiltration in human pancreatic cancer.

(A) PCA analysis comparing intensity of marker staining of n=8 normal or adjacent pancreata tissue samples (blue) compared to n=9 PDA tumor samples (red). **(B)** Merged adj/norm panc (left) and PDA (right) t-SNE analysis of defined cell clusters from CyTOF analysis on tissue samples. The size of the dot represents the number of cells in the cluster. Each color represents a cell population: CD4 T cells (red), CD8 T cells (pink), B cells (blue), Myeloid (light orange), Macrophages (orange), $CD45^-$ cells (light purple), Unknown (purple). **(C)** Bar plot representation from FlowSOM CyTOF analysis of n=8 adj/norm tissue samples and n=9 PDA tumor samples. Analysis was only performed on samples with greater than 3,000 live singlets. **(D)** Manual quantitation of total immune cells ($CD45^+$), myeloid cells ($CD11b^+$), $CD4^+$ T cells, $CD8^+$ T cells, potential Tregs ($CD4^+$ $CD25^+$), and B

cells. Manual gating included n=8 adj/norm patients and n=10 PDA patients per group. Asterisk denotes a p-value less than 0.05 determined by two-sided Student's t-test. **(E)** Correlation plot of total $CD11b^+$ myeloid cells compared to total $CD8^+$ T cells. **(F)** mfIHC composite images of formalin-fixed, paraffin-embedded tissue specimens from four different patients with chronic pancreatitis (top row) and four patients with PDA (bottom row). Antibodies and colors are as follows: CD163 (orange), PD-L1 (magenta), Pancytokeratin (PanCK; white), CD3 (green), CD8 (yellow), FOXP3 (red), and DAPI (blue). **(G)** Comparison of cellular infiltration between n=34 chronic pancreatitis patients and n=71 PDA patients (P-values: Other 0.0001, $CD163^+$ cells 0.020, $CD8^+$ T cells 0.3483, Treg <0.0001, Epithelial <0.0001). **(H)** Correlation between percentage of $CD8^+$ T cells and $CD163^+$ cells in chronic pancreatitis and PDA.

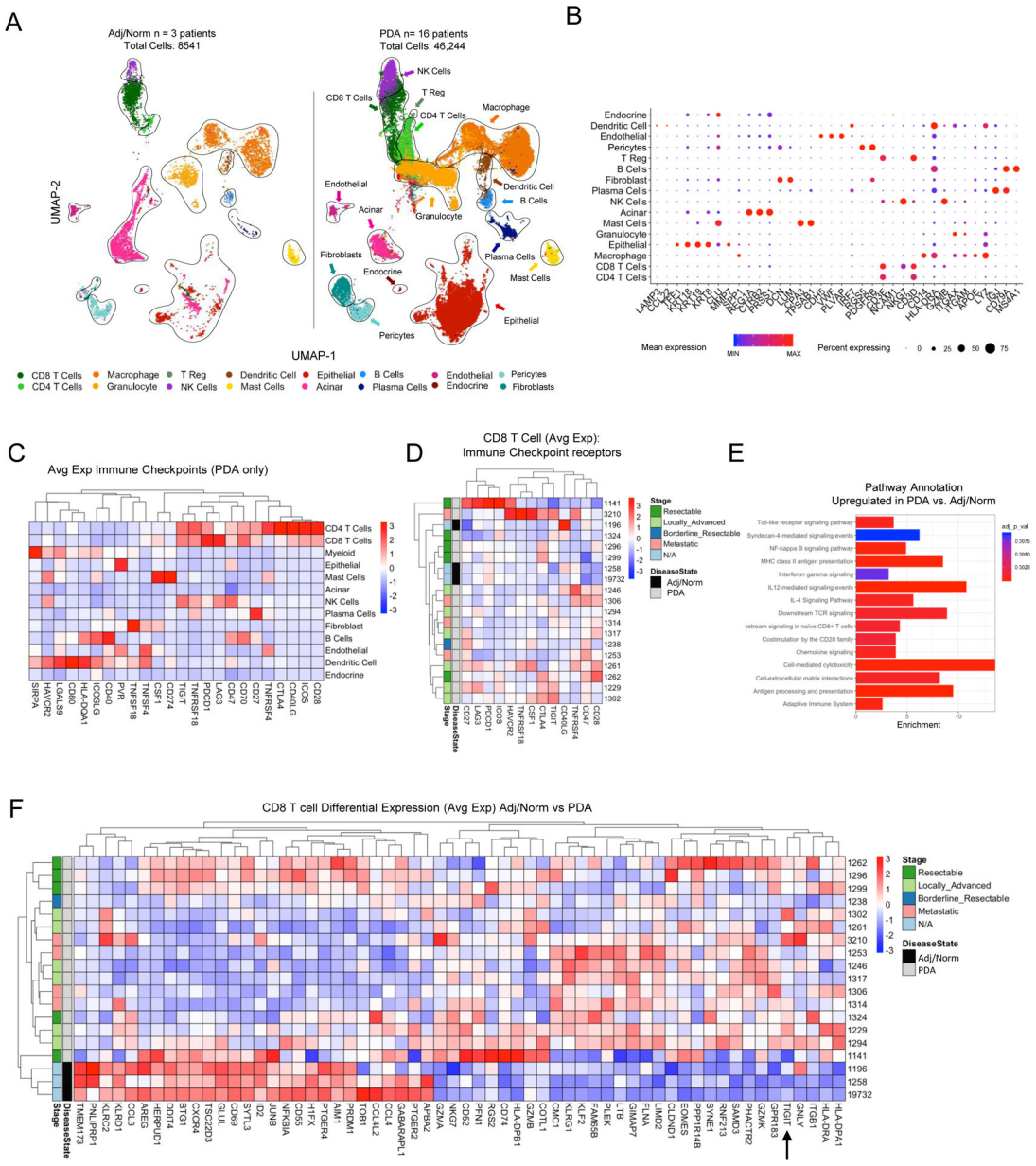

Figure 2. Single cell RNA sequencing reveals heterogenous expression of immune checkpoints in PDA tissue.

(A) UMAP on 3 adjacent/normal pancreas (left) and 16 PDA patient (right) tissues. Populations identified as follows: acinar (pink), epithelial (red), fibroblasts (dark and light teal), $CD8^+$ T cells (dark green), $CD4^+$ T cells, (neon green), Tregs (light green), NK cells (purple), B cells (light blue), plasma cells (dark blue), mast cells (yellow), macrophages (dark orange), granulocytes (light orange), dendritic cells (brown), endothelial cells (dark pink), and endocrine (dark red). **(B)** Dot plot of key markers used to define the identified cell populations. Color of dot represents average expression, while the size of the dot represents percent expression. Dot plot represents merged n=3 adj/norm patients and n=16 PDA patients gene expression of lineage markers. **(C)** Average expression of immune checkpoint ligands and receptors in the identified cell populations in n=16 tumor tissue samples. **(D)**

Average expression of immune checkpoint receptors on $CD8^+$ T cells in n=16 PDA patients and n=3 adj/norm patients merged tissues. **(E)** Pathway annotations from gene set enrichment analysis (GSEA) using the R package *clusterprofiler* in n=16 PDA samples compared to n=3 adj/norm samples. The color of the bar represents the p-value adjusted for multiple comparisons using the Benjamini Hochberg method. Enrichment score is plotted on the x-axis. **(F)** Unbiased differential expression between $CD8^+$ T cells from adj/norm pancreas (black) and PDA (grey). Significantly up- and down-regulated genes are plotted as average expression per patient. This analysis was performed on all $CD8^+$ T cells found in the adjacent/normal and PDA tissue. Disease stage is plotted on the left: resectable (green), locally advanced (light green), borderline resectable (blue), metastatic (pink), N/A (light blue).

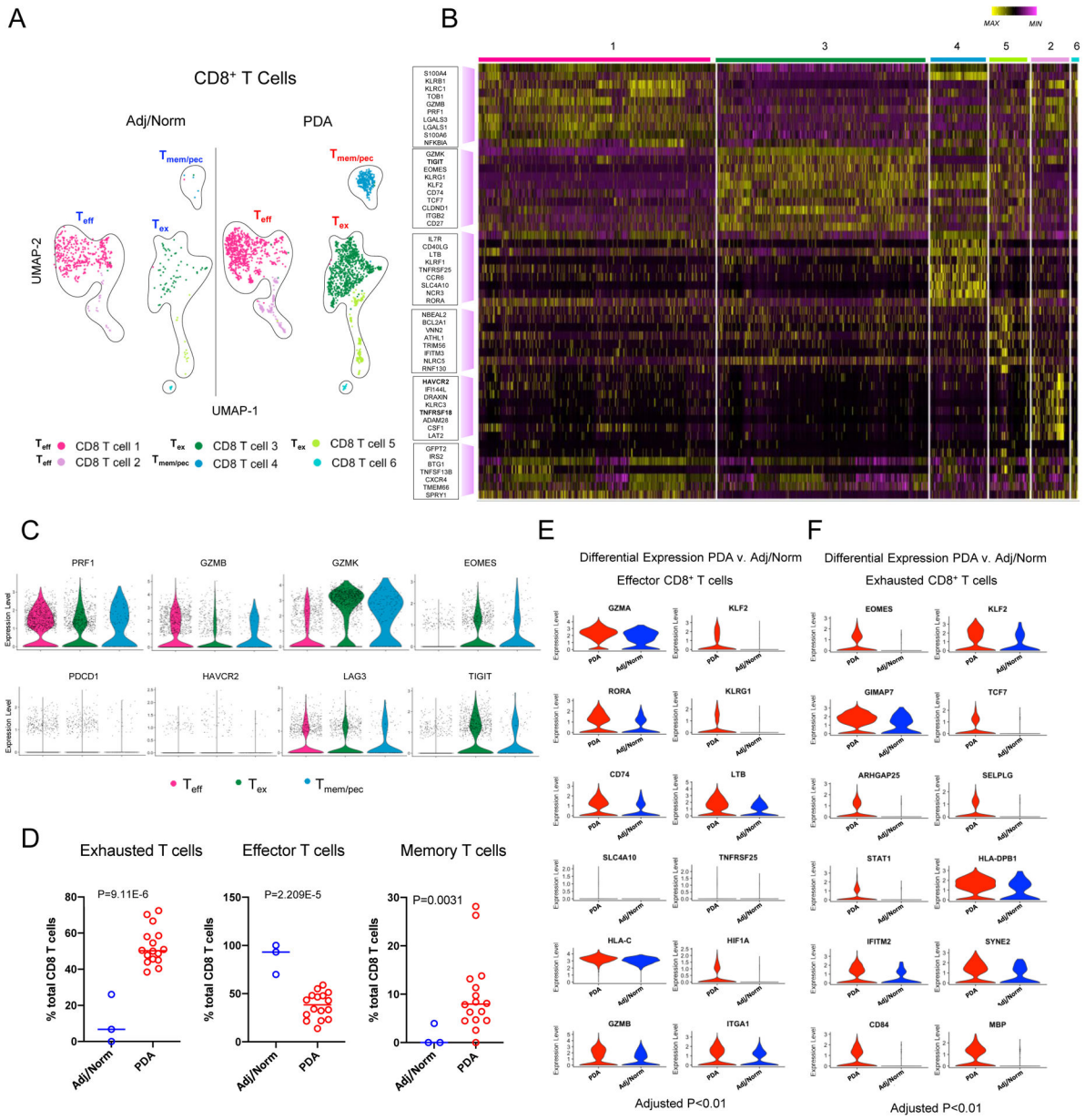

Figure 3. Single cell RNA sequencing reveals exhausted CD8$^+$ T cell phenotype in PDA patients is defined by the immune checkpoint *TIGIT*.

(A) UMAP analysis of CD8$^+$ T cells from n=3 adjacent/normal pancreas samples (left) and n=16 PDA tumors (right). The 6 identified subsets of CD8$^+$ T cells were collapsed into potential memory (blue), effector (pink) and exhausted (green). **(B)** Single cell resolution heatmap analysis of top 10 genes for each identified CD8$^+$ T cell subset. **(C)** Violin plots of normalized expression for selected markers mapped across the CD8$^+$ T cell subsets. **(D)** Quantitation of potential exhausted (p=9.11E-6), effector (p=2.209E-5) and memory (p=0.0031) T cells in adjacent/normal pancreas and PDA patients, plotted as % total CD8$^+$ T cells. Plots represent n=3 adj/norm and n=16 PDA patients. Two-sided Student's *t*-test was performed to compare between groups and a p value of 0.05 or less was considered statistically significant. Panel of genes differentially expressed in **(E)** effector and **(F)**

exhausted $CD8^+$ T cells in PDA (red) compared to adjacent/normal pancreas (blue). Plots represent n=3 adj/norm and n=16 PDA patients. Violin plots are shown as normalized expression. All violin plots in (E) and (F) have an adjusted p-value of $p<0.01$ and are considered statistically significant.

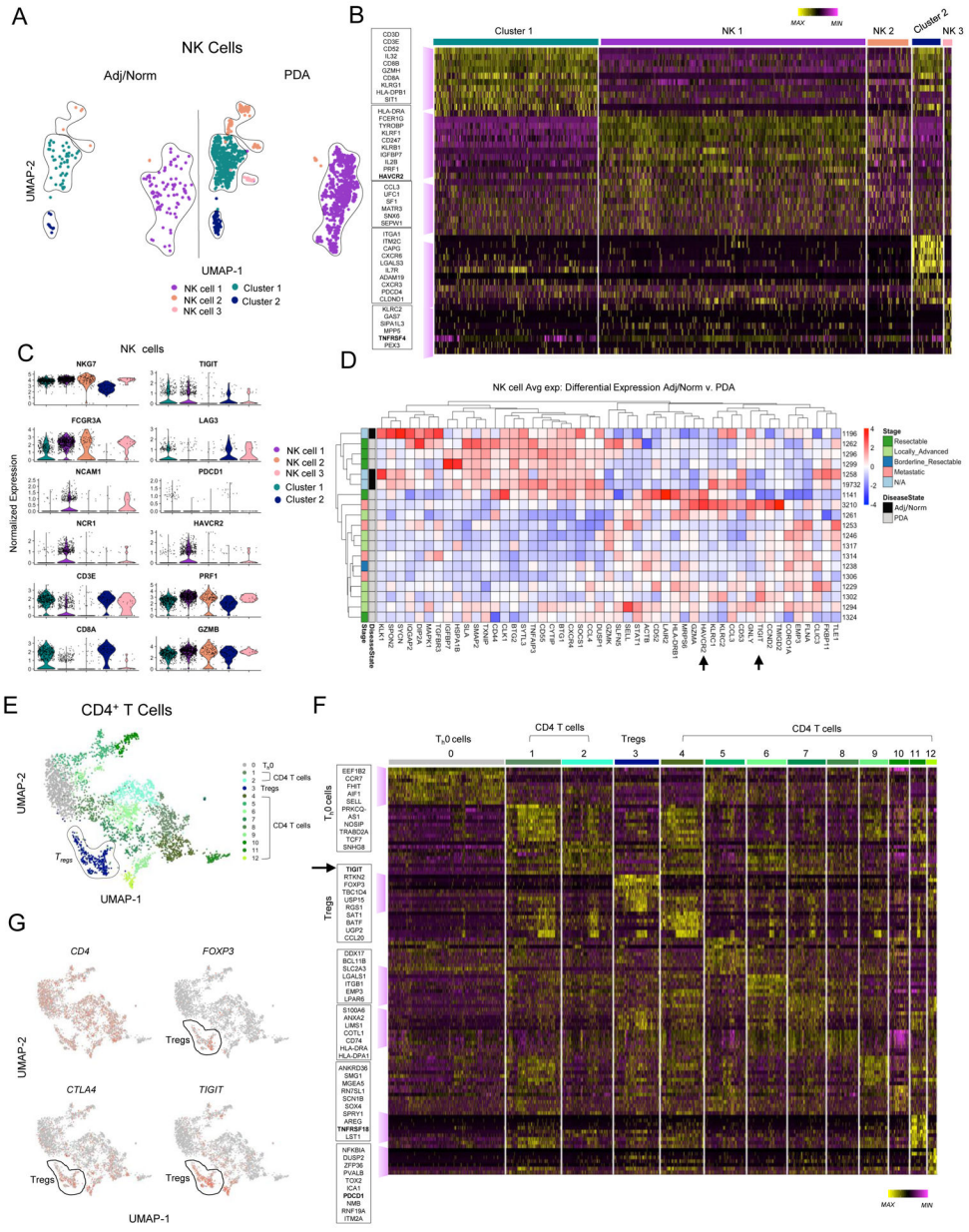

Figure 4. Single cell RNA sequencing of pancreatic tissues reveals *TIGIT* is differentially expressed in NK cells from PDA patients and is a defining marker of Tregs.

(A) Merged UMAP of 5 identified subsets of NK cells from adjacent/normal pancreas (left) and PDA (right). Plots represent n=3 adj/norm and n=16 PDA patients. **(B)** Single cell resolution heatmap of each NK cell subset identified. Immune checkpoints (*HAVCR2, TNFRSF4)* are bolded. **(C)** Violin plots of normalized average expression within NK cell subsets demonstrating specific lineage markers for NK cells (such as *NCAM1/FCGR3A*) and immune checkpoint receptors. **(D)** Unbiased differential average expression of merged NK cells from adjacent/normal pancreas (black) and PDA (grey). Disease stage is plotted on the left. **(E)** Merged UMAP of all CD4$^+$ T cells with 13 identified cell subsets. Naïve CD4$^+$ T cells are denoted as T_h0 (*CCR7*$^+$) and Tregs as Tregs (*FOXP3*$^+$). All other subsets are denoted as CD4 T cells. **(F)** Single cell resolution heatmap of each CD4$^+$ T cell subset.

Boxes on the left designate naïve $CD4^+$ T cells (T_h0) and the $CD4^+$ T cell subsets that are defined by immune checkpoint expression (*TIGIT, TNFRSF18, PDCD1*). **(G)** Feature plots of *CTLA4* and *TIGIT* in regulatory $CD4^+$ T cells (outlined). In all panels, plots represent n=3 adj/norm and n=16 PDA patients.

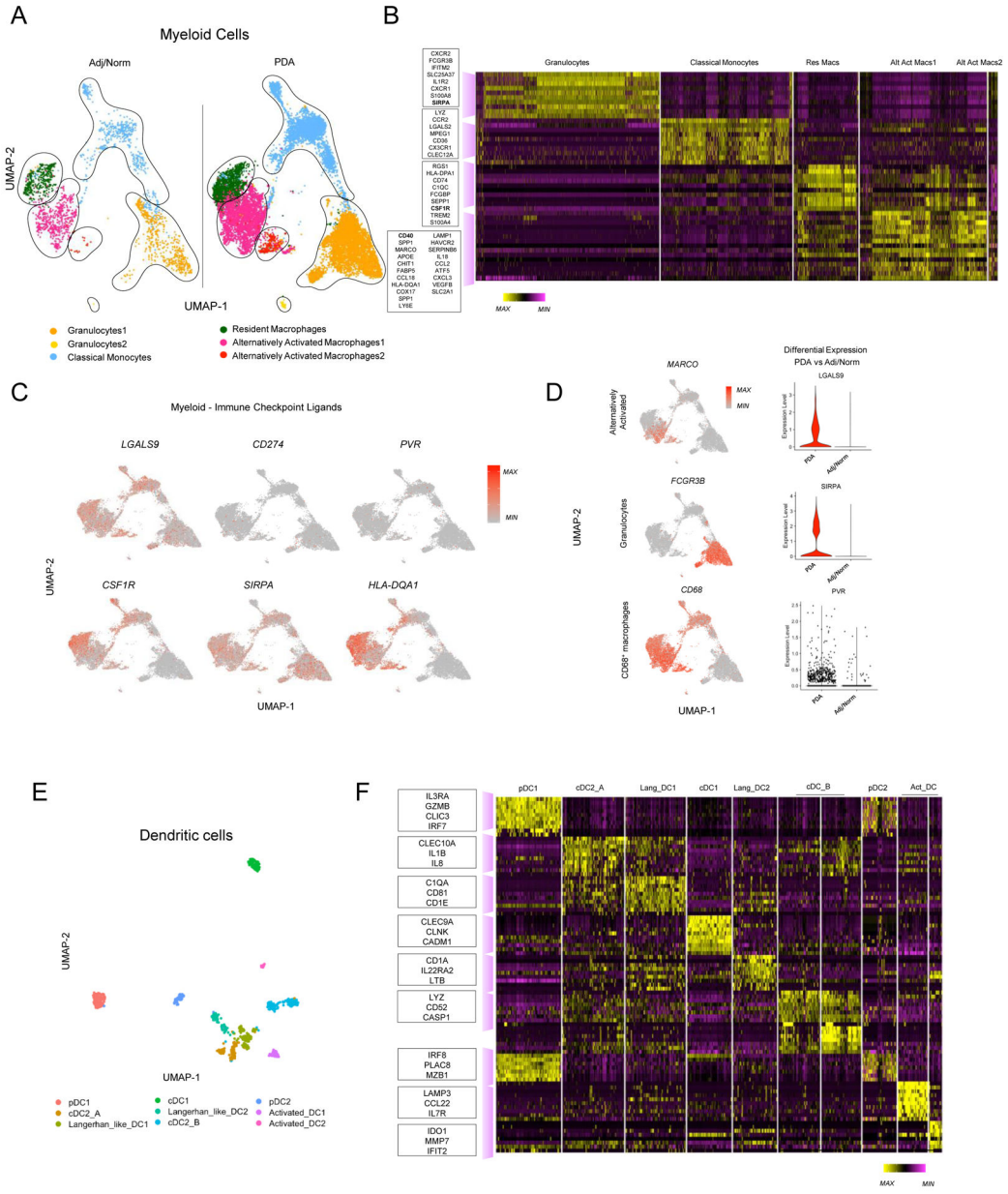

Figure 5. Single cell RNA sequencing reveals distinct myeloid and dendritic cell subsets.

(A) Merged UMAP of 6 identified myeloid cell subsets in adjacent/normal pancreas (left) and PDA (right). **(B)** Single cell resolution heatmap of each myeloid cell subset identified. Boxes on the left designate the top expressing genes for each myeloid subset. **(C)** Selected feature plots of the immune checkpoints, *LGALS9, CD274, PVR, CSF1R, SIRPA, HLA-DQA1* in myeloid cells. **(D)** Selected feature plots of markers that define alternatively activated macrophages, granulocytes, and total macrophage subsets (left) and violin plots of immune checkpoint ligands that are upregulated in PDA patients (right). **(E)** UMAP analysis of dendritic cells in merged normal/adjacent pancreas and PDA. **(F)** Top ten highly enriched gene signature analysis of dendritic cell subclusters identifying potential DC subsets, including plasmocytoid DCs (pDCs), Langerhans-like DCs (Lang_DCs), conventional DCs

(cDCs), and activated DCs (Act_DCs). In all panels, plots represent n=3 adj/norm and n=16 PDA patients.

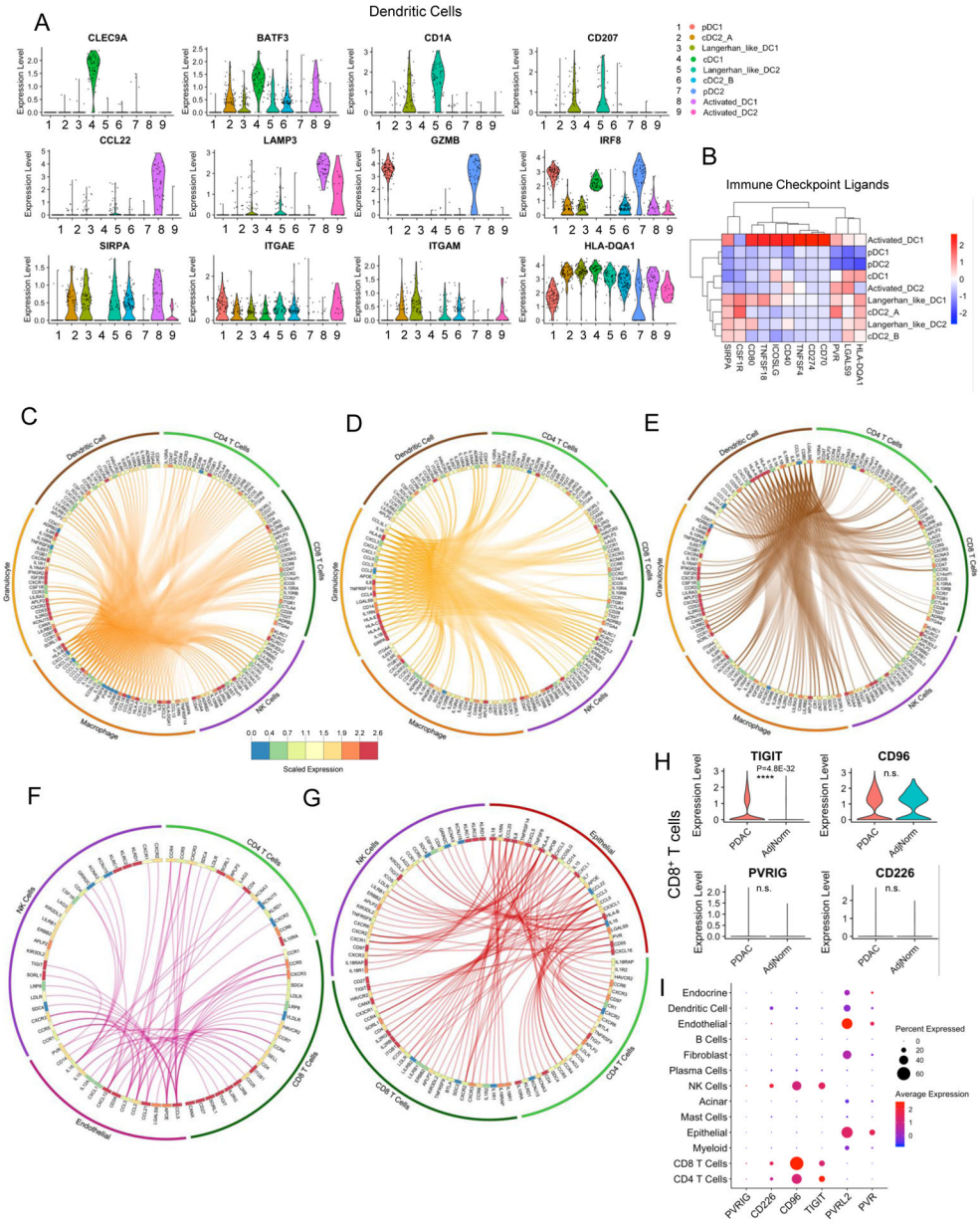

Figure 6. Predicted ligand receptor mapping in PDA patients demonstrate myeloid and non-immune cell types as sources of immune checkpoint ligands.

(A) Violin plots, where each dot represent a single cell, of select dendritic cell lineage markers across all 9 identified subsets. **(B)** Immune checkpoint ligand expression heatmap within dendritic subclusters. **(C)** Circos plot map of all putative ligand receptor interactions that are upregulated in PDA macrophages, **(D)** granulocytes, **(E)** dendritic cells, **(F)** endothelial cells **(G)** epithelial cells compared to adjacent/normal pancreas visualized by circos plot using the Circos software V0.69-9 (circos.ca). The heatmap within the circos plots is the scaled average expression of each gene within PDA tissue cell populations. The interactions plotted are those in which the expression level of either the ligand, the receptor, or both are increased in expression in PDA samples compared to adjacent/normal tissue. **(H)** Violin plots for the normalized expression of *TIGIT*, *CD96*, and *CD226* in $CD8^+$ T cells in

PDA (red) compared to adjacent/normal pancreas (blue). Between adj/norm and PDA groups, the asterisk indicates P<0.0001, and exact P=4.8E-32. For Figure 6 panels A through H, n=3 adj/norm samples were examined and n=16 PDA patients were analyzed. **(I)** Dot plot analysis of TIGIT family members within PDAC tissue. Color of dot represents average expression, while the size of the dot represents percent expression. Dot plot represent n=16 PDA patients gene expression.

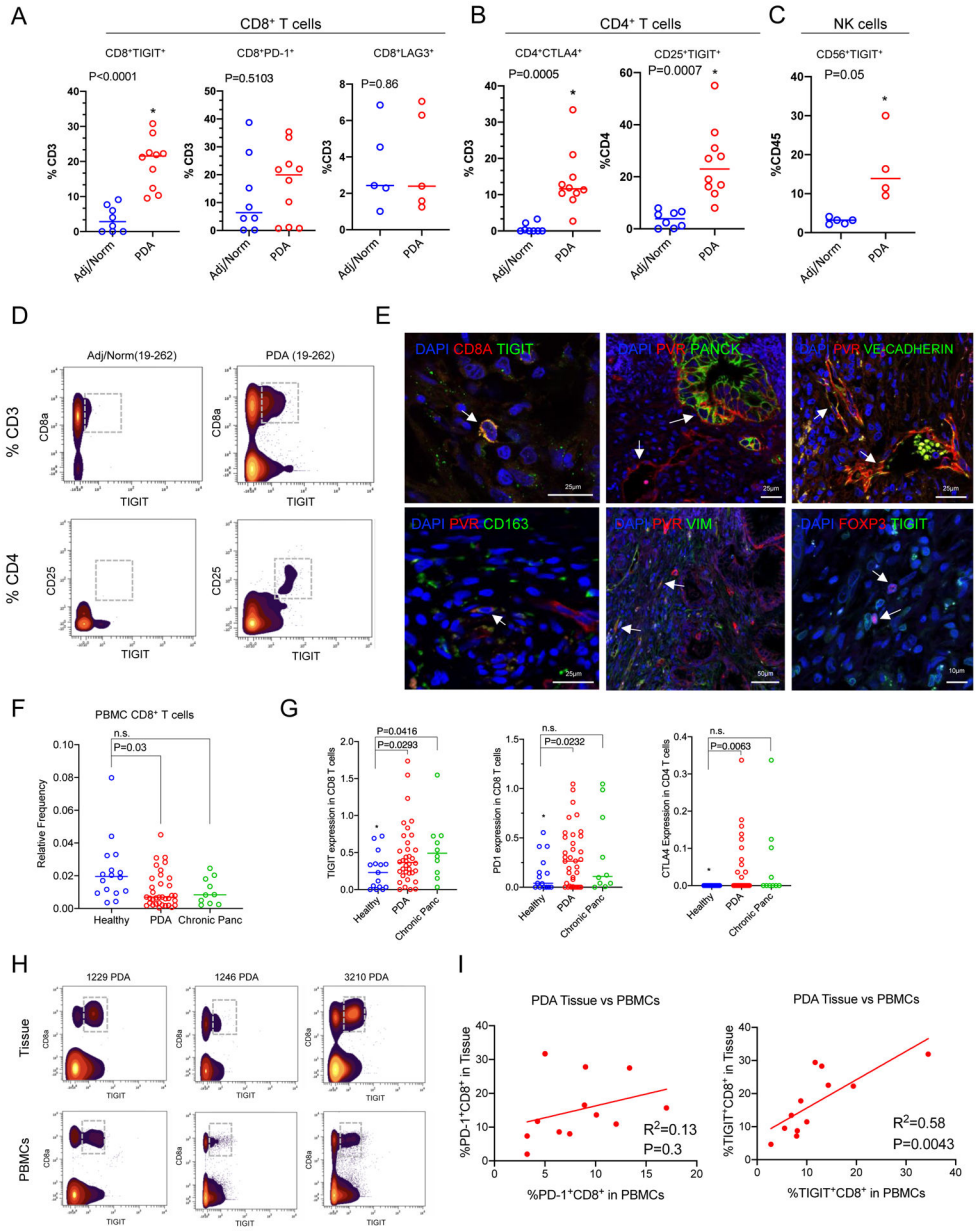

Figure 7. CyTOF and immunofluorescence protein validation of immune checkpoint expression in human pancreatic tissues and PBMCs.

Manual gating of CyTOF for immune checkpoints, including **(A)** TIGIT (n=8 adj/norm pancreas samples, n=10 PDA tumors), PD-1 (n=8 adj/norm pancreas samples, n=10 PDA tumors), and LAG3 (n=5 adj/norm pancreas samples, n=5 PDA tumors) in $CD8^+$ T cells, **(B)** CTLA4 in $CD4^+$ T cells (n=8 adj/norm pancreas samples, n=10 PDA tumors) and TIGIT in $CD25^+$ $CD4^+$ potential Tregs (n=8 adj/norm, n=10 PDA), and **(C)** $CD56^+$ NK cells in n=5 adjacent/normal pancreas samples and n=4 PDA tumor tissues. In Figure 7A–C two-sided Student's *t*-tests were performed and a p value of <0.05 was considered statistically significant. **(D)** Representative individual CyTOF biaxial density plots from normal adjacent and PDA tissue of a matched patient (19–262) of TIGIT expression in both CD8 T cells (as a percentage of total $CD3^+$ cells) and $CD25^+$ potential Tregs (as a percentage of $CD4^+$ cells).

(E) PDA patient tissues, where 3 individual patient tumors were examined independently per staining analysis, were stained with antibodies against TIGIT with either CD8A ($CD8^+$ T cells) or FOXP3 (Tregs), and PVR with Pan-cytokeratin (epithelial cells), VE-cadherin (endothelial cells), CD163 (myeloid), or Vimentin (fibroblasts). **(F)** Quantitation of the percentage of $CD8^+$ T cells (of total live cells) from CyTOF of healthy, PDA, and chronic pancreatitis patient PBMCs. Quantitation of PBMC CyTOF data represent n=16 healthy, n=36 PDA, and n=10 chronic pancreatitis patients. In the healthy versus chronic pancreatitis comparison, the n.s. P value = 0.0702. **(G)** TIGIT and PD-1 transformed protein expression within $CD8^+$ T cells of healthy, PDA, and chronic pancreatitis patient PBMCs, and for the comparison between healthy and the chronic pancreatitis patients the n.s. P=0.1224. CTLA4 expression in $CD4^+$ T cells of healthy (n=16), PDA (n=36), and chronic pancreatitis (n=10) patient PBMCs, and for the comparison between healthy and the chronic pancreatitis patients the n.s. P=0.1216. In Figure 7F–G two-sided Student's *t*-tests were performed and a p value of <0.05 was considered statistically significant. **(H)** Representative biaxial plots of TIGIT expression in $CD8^+$ T cells in the tumor tissue and matched blood of three PDA patients (1229, 1246, 3210). **(I)** Correlation of CyTOF data from PDA patient tissue versus matched PBMC $CD8^+$ T cells expressing TIGIT and PD-1 (of total $CD3^+$ cells).